Effect of charge-transfer enhancement on the efficiency and rotary mechanism of an oxindole-based molecular motor

Daisy R. S. Pooler[†[a]], Robin Pierron[†[b]], Stefano Crespi[†[a]], Romain Costil[[a]], Lukas Pfeifer[[a]], Jérémie Léonard*[[b]], Massimo Olivucci*[[c,d]], and Ben L. Feringa*[[a]]

[a] Stratingh Institute for Chemistry, Zernike Institute for Advanced Materials, University of Groningen, Nijenborgh 4, 9747 AG Groningen, The Netherlands

[b] Institut de Physique et Chimie des Matériaux de Strasbourg, Université de Strasbourg & CNRS, UMR 7504, F-67034 Strasbourg, France,

[c] Dipartimento di Biotecnologie, Chimica e Farmacia, Università di Siena, 53100 Siena, Italy

[d] Chemistry Department, Bowling Green State University, Bowling Green Ohio 43403, USA

† These authors contributed equally

Correspondence should be addressed to:

J. Léonard, Email: jeremie.leonard@ipcms.unistra.fr

M. Olivucci, Email: massimo.olivucci@unisi.it, molivuc@bgsu.edu

B. L. Feringa, E-mail: b.l.feringa@rug.nl

1. Table of Contents

1. General synthetic procedures

All reactions involving air sensitive reagents were performed under an N_2 atmosphere. Solvents were degassed by purging with N_2 for a minimum of 30 min or by three freeze-pump-thaw cycles. Reagents were purchased from Sigma Aldrich, Acros or TCI Europe and were used as received. Solvents were reagent grade and used without prior water removal unless otherwise indicated. Anhydrous THF was obtained from a solvent purification system (MBraun SPS-800). Flash column chromatography was performed on silica gel (Merck, type 9385, 230–400 mesh) or on a Büchi Reveleris purification system using Büchi silica cartridges. Thin layer chromatography (TLC) was carried out on aluminium sheets coated with silica gel 60 F254 (Merck). Compounds were visualised with a UV lamp (254 nm) and/or by staining with $KMnO_4$ or Cerium Ammonium Molybdate.

^1H and ^{13}C NMR spectra were recorded on a Varian Mercury-Plus 400 or a Bruker Avance 600 NMR spectrometer at 298 K unless otherwise indicated. PSS studies were performed on a Varian Unity Plus 500 NMR spectrometer. Chemical shifts are given in parts per million (ppm) relative to the residual solvent signal (for $CDCl_3$ δ 7.26 for 1H, δ 77.16 for 13C and for CD_2Cl_2 δ 5.32 for ^1H, δ 53.84 for ^{13}C). Multiplets in ^1H NMR spectra are designated as follows: s (singlet), d (doublet), t (triplet), q (quartet), p (pentet), m (multiplet), br (broad). High resolution mass spectrometry (ESI+) was performed on an LTQ Orbitrap XL spectrometer.

Analytical chromatography was performed on a Shimadzu Prominence HPLC system. Enantiomers of ***E*s-1** and ***Z*s-1** were separated on a Daicel CHIRALPAK OD-H analytical column with Heptane/Propan-2-ol 90:10 eluant, at a 0.5 ml/min flux.

2. Preparation and characterisation of compounds

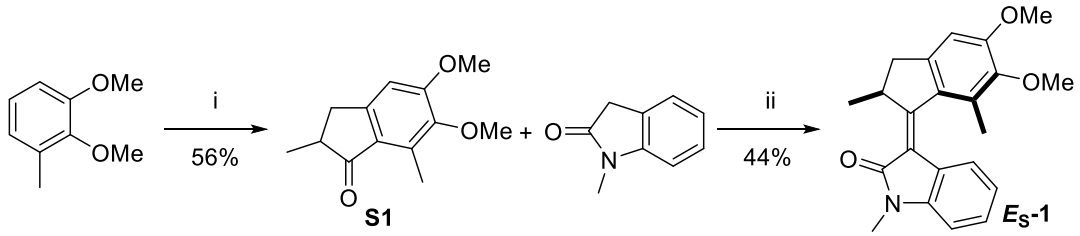

Figure S1. Synthesis of motor **1** in its stable *E* form. i) Methacrylic acid (1.7 equiv.), PPA (115% H_3PO_4), 70 °C, 3 h. ii) $TiCl_4$ (1.5 equiv.), DBU (1.5 equiv.), THF, 0 °C – rt, 4 h.

5,6-dimethoxy-2,7-dimethyl-2,3-dihydro-1H-inden-1-one (S1)

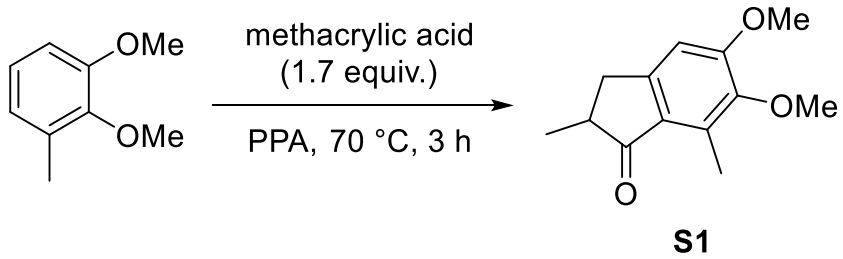

S1

To a round-bottom flask equipped with a mechanical stirrer was added polyphosphoric acid (PPA, 115% H_3PO_4, 60 mL), heated to 70 °C and then was added methacrylic acid (25.4 mL, 300 mmol, 1.7 equiv.) and 2,3-dimethoxytoluene (26.4 mL, 178 mmol, 1.0 equiv.). After stirring at 70 °C for 3 h, the mixture was allowed to cool to room temperature, quenched by adding ice and was mechanically stirred overnight. The mixture was extracted with EtOAc (3 x 100 mL), and the combined organic layers were washed with saturated aq. $NaHCO_3$ (50 mL) and brine (50 mL), dried over $MgSO_4$ and the solvent was evaporated *in vacuo* to a light brown solid. The crude product was recrystallized from hot heptane to yield **S1** (21.8 g, 99.0 mmol, 56%) fluffy brown crystals. Data is in accordance with literature.[1]

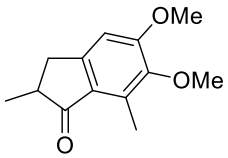

S1

^{1}H NMR (400 MHz, $CDCl_3$) δ 6.74 (s, 1H, Ar*H*), 3.92 (s, 3H, OC*H*$_3$), 3.76 (s, 3H, OC*H*$_3$), 3.25 (dd, J = 16.4, 7.4 Hz, 1H, C*H*$_A$H$_B$), 2.70 – 2.60 (m, 2H, CH$_A$*H*$_B$ + C*H*CH$_3$), 2.55 (s, 3H, ArC*H*$_3$), 1.27 (d, J = 7.3 Hz, 3H, CHC*H*$_3$); **^{13}C NMR** (101 MHz, $CDCl_3$) δ 209.1 (*C*=O), 158.2 (*C*), 152.0 (*C*), 146.9 (*C*), 132.2 (*C*), 127.4 (*C*), 106.0 (*C*H), 60.5 (O*C*H$_3$), 55.9 (O*C*H$_3$), 42.7 (*C*HCH$_3$), 34.6 (*C*H$_2$), 16.7 (CH*C*H$_3$), 10.8 (Ar*C*H$_3$).

(*E*)-3-(5,6-dimethoxy-2,7-dimethyl-2,3-dihydro-1H-inden-1-ylidene)-1-methylindolin-2-one (*E*s-1)

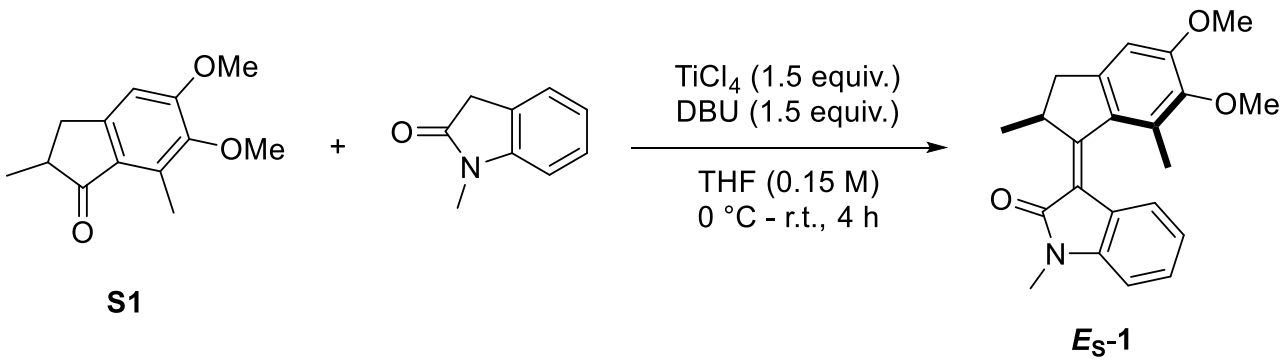

An oven-dried Schlenk tube under N_2 atmosphere was charged with **S1** (100 mg, 0.45 mmol, 1.0 equiv.) and dry THF (2 mL, 0.22 M), and cooled to 0 °C in an ice bath. $TiCl_4$ (0.8 mL, 0.68 mmol, 1.5 equiv.) was added dropwise and the resulting suspension was stirred for 5 min at this temperature. To this mixture was added a solution of *N*-methyloxindole (100 mg, 0.68 mmol, 1.5 equiv.) in dry THF (1 mL, 0.68 M) *via* syringe, and was stirred for 30 min at 0 °C. Subsequently, DBU (0.10 mL, 0.68 mmol, 1.5 equiv.) was added dropwise, and the resulting mixture was allowed to warm to room temperature and stirred for 4 h. The reaction was quenched with 1 M aqueous HCl solution and extracted with EtOAc (3 x 10 mL). The combined organic layers were washed with brine and dried over $MgSO_4$, and the volatiles removed *in vacuo* to give a yellow oil, which was purified by flash column chromatography (SiO_2, pentane:EtOAc 4:1), and subsequently recrystallized from EtOAc to yield motor ***E*s-1** (70 mg, 0.20 mmol, 44%) as bright orange crystals.

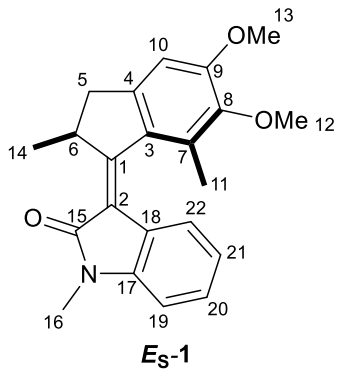

^{1}H NMR (400 MHz, $CDCl_3$) δ 7.20 (td, J = 7.6, 1.1 Hz, 1H, H_{21}), 7.02 (d, J = 7.6 Hz, 1H, H_{22}), 6.89 (td, J = 7.6, 1.1 Hz, 1H, H_{20}), 6.86 (s, 1H, H_{10}), 6.82 (d, J = 7.6 Hz, 1H, H_{19}), 4.39 (dq, J = 6.3, 6.7 Hz, 1H, H_6), 3.95 (s, 3H, H_{13}), 3.86 (s, 3H, H_{12}), 3.31 (s, 3H, H_{16}), 3.23 (dd, J = 15.1, 6.3 Hz, 1H, H_5), 2.55 (d, J = 15.1 Hz, 1H, H_5), 2.18 (s, 3H, H_{11}), 1.22 (d, J = 6.7 Hz, 3H, H_{14}); **^{13}C NMR** (151 MHz, $CDCl_3$) δ 168.6 (C_{15}), 163.3 (C_1), 155.2 (C_9), 147.0 (C_8), 145.9 (C_4), 142.2 (C_{17}), 132.0 (C_3), 131.6 (C_7), 127.5 (C_{21}), 122.9 (C_{18}), 122.2 (C_{22}), 120.9 (C_{19}), 118.4 (C_2), 107.3 (C_{20}), 107.0 (C_{10}), 60.2 (C_{12}), 55.8 (C_{13}), 43.4 (C_6), 41.1 (C_5), 25.8 (C_{16}), 19.2 (C_{14}), 16.0 (C_{11}); **HRMS** (ESI+, *m/z*) calcd for $C_{22}H_{23}NO_3$ $[M+H]^+$ = 350.1751, found 350.1747.

(*Z*)-3-(5,6-dimethoxy-2,7-dimethyl-2,3-dihydro-1H-inden-1-ylidene)-1-methylindolin-2-one (Zs-1)

***E*s-1** (70 mg, 200 µmol) was dissolved in CH_2Cl_2 (20 mL, 0.01 M) and left under ambient light for 24 h at room temperature. The volatiles were removed *in vacuo*, and the resulting yellow oil was purified by flash column chromatography (SiO_2, pentane:EtOAc 99:1 – 80:20), and subsequently recrystallized from EtOAc to yield ***Z*s-1** (16 mg, 46 µmol, 23%) as bright orange crystals.

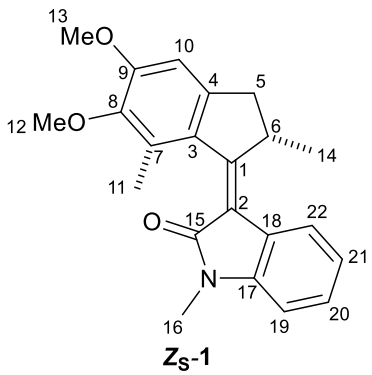

Zs-1

^{1}H NMR (400 MHz, $CDCl_3$) δ 7.54 (d, J = 7.6 Hz, 1H, H_{22}), 7.31 – 7.22 (m, overlaps $CDCl_3$, 1H, H_{21}), 7.07 (td, J = 7.8z, 1.2 Hz, 1H, H_{20}), 6.86 (d, J = 7.8 Hz, 1H, H_{19}), 6.76 (s, 1H, H_{10}), 3.90 (s, 3H, H_{13}), 3.88 (s, 3H, H_{12}), 3.89 – 3.82 (m, overlaps H_{12}, 1H, H_6), 3.27 (s, 3H, H_{16}), 3.24 (dd, J = 14.9, 6.8 Hz, overlaps H_{16}, 1H, H_5) 2.55 (d, J = 14.9 Hz, 1H, H_5), 2.32 (s, 3H, H_{11}), 1.31 (d, J = 6.8 Hz, 3H, H_{14}); **^{13}C NMR** (151 MHz, $CDCl_3$) δ 165.6 (C_{15}), 162.1 (C_1), 155.3 (C_9), 146.5 (C_8), 144.5 (C_{17}), 142.5 (C_4), 135.3 (C_3), 131.3 (C_7), 127.3 (C_{20}), 124.6 (C_{18}), 122.3 (C_{22}), 121.4 (C_{21}), 118.3 (C_{18}), 107.6 (C_{19}), 106.0 (C_{10}), 60.4 (C_{12}), 55.8 (C_{13}), 44.1 (C_6), 40.8 (C_5), 26.0 (C_{16}), 19.4 (C_{14}), 15.7 (C_{11}); **HRMS** (ESI+, *m/z*) calcd for $C_{22}H_{23}NO_3$ $[M+H]^+$ = 350.1751, found 350.1755.

2. NMR spectra

(*E*)-3-(5,6-dimethoxy-2,7-dimethyl-2,3-dihydro-1H-inden-1-ylidene)-1-methylindolin-2-one (*E*s-1) ($CDCl_3$)

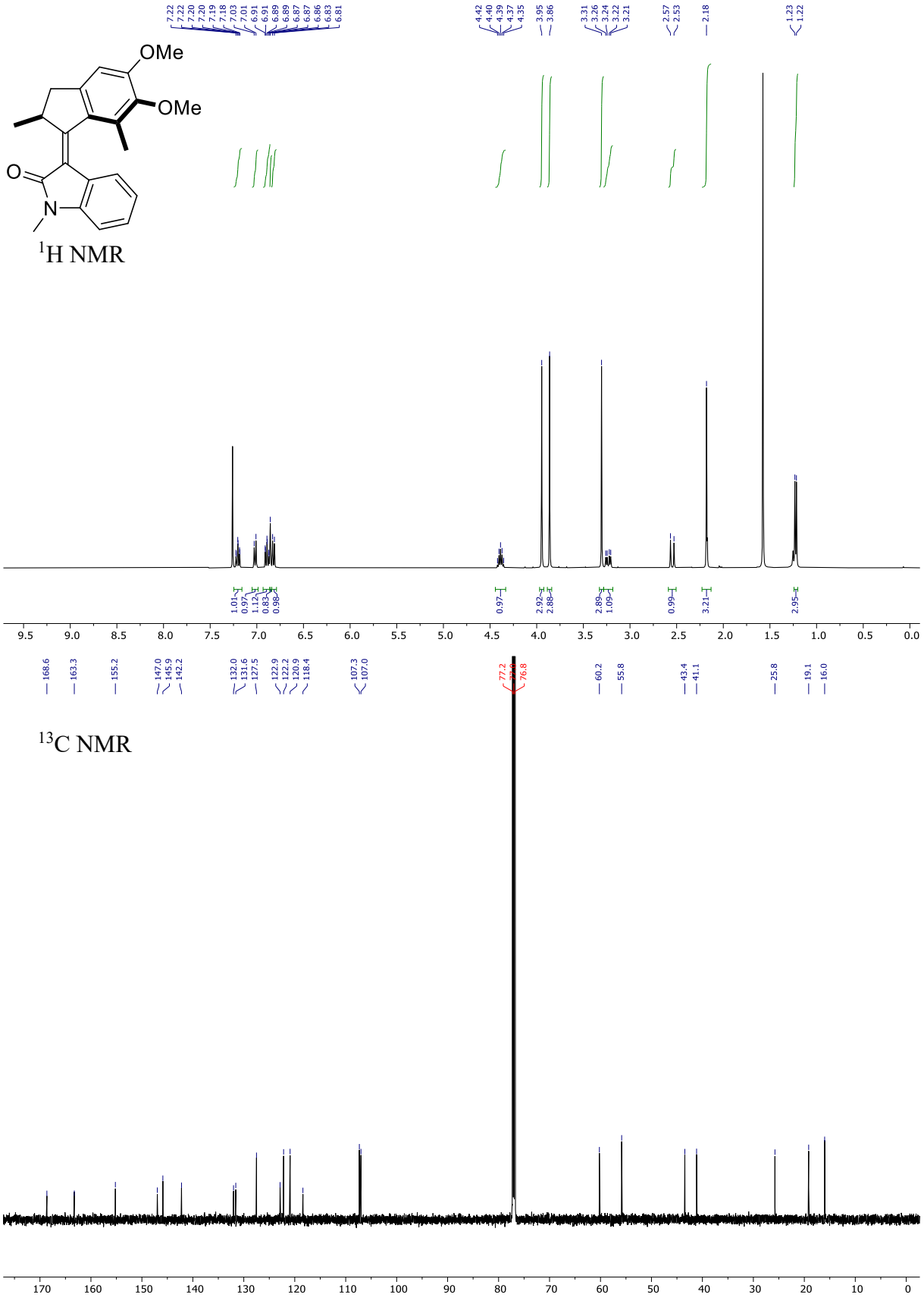

^{1}H NMR

^{13}C NMR

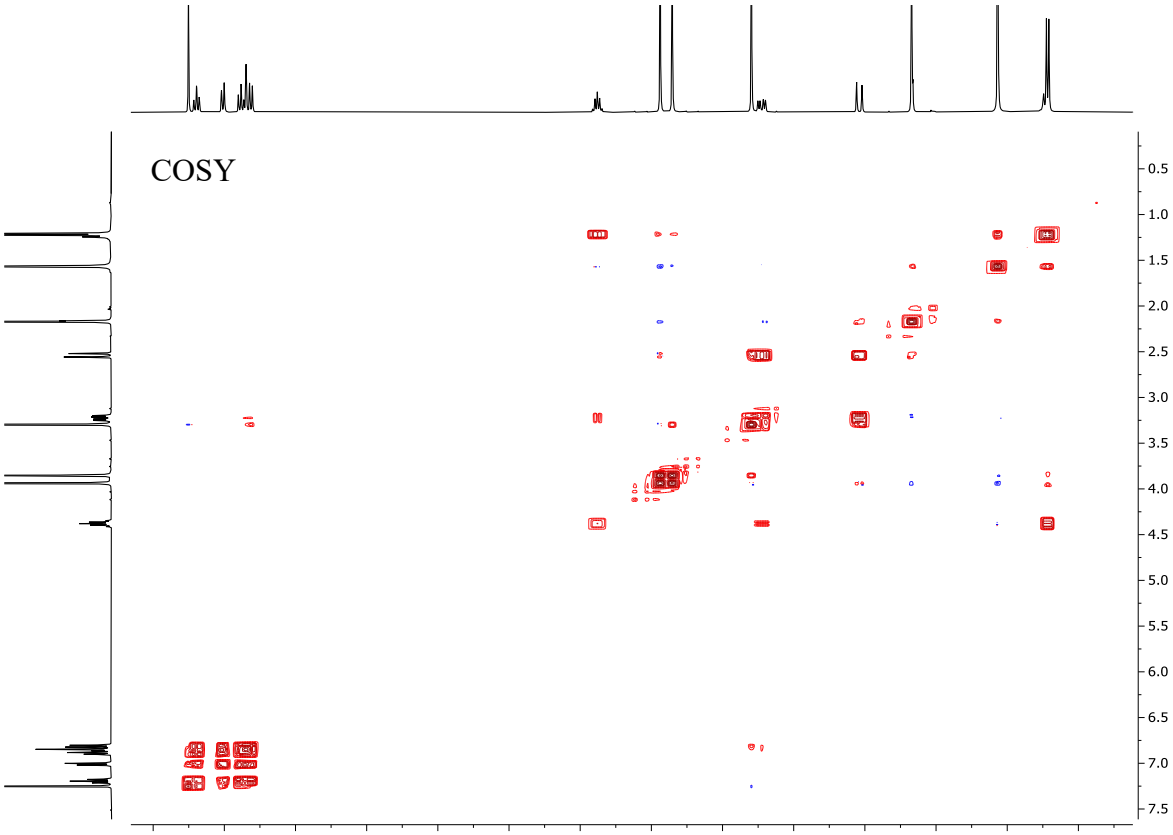
COSY
7.5
7.0
6.5
6.0
5.5
5.0
4.5
4.0
3.5
3.0
2.5
2.0
1.5
1.0
0.5

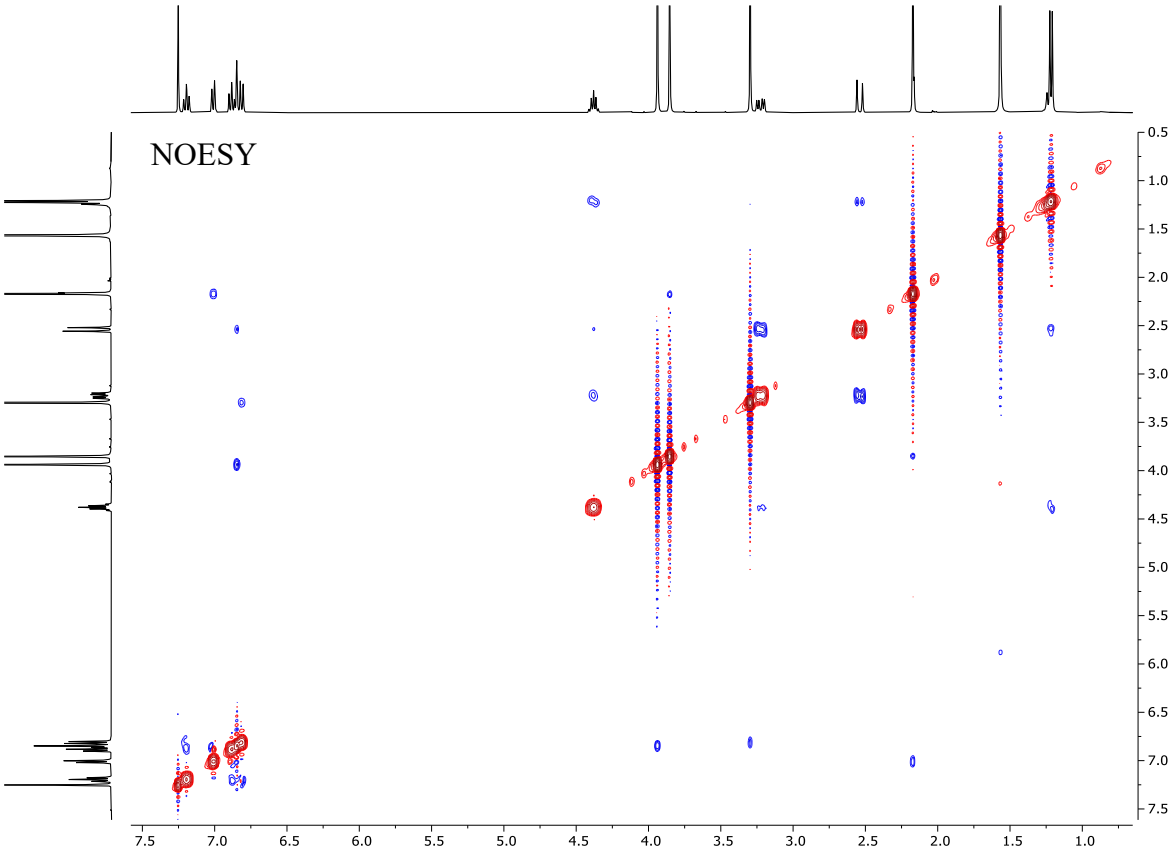
NOESY
7.5
7.0
6.5
6.0
5.5
5.0
4.5
4.0
3.5
3.0
2.5
2.0
1.5
1.0
0.5

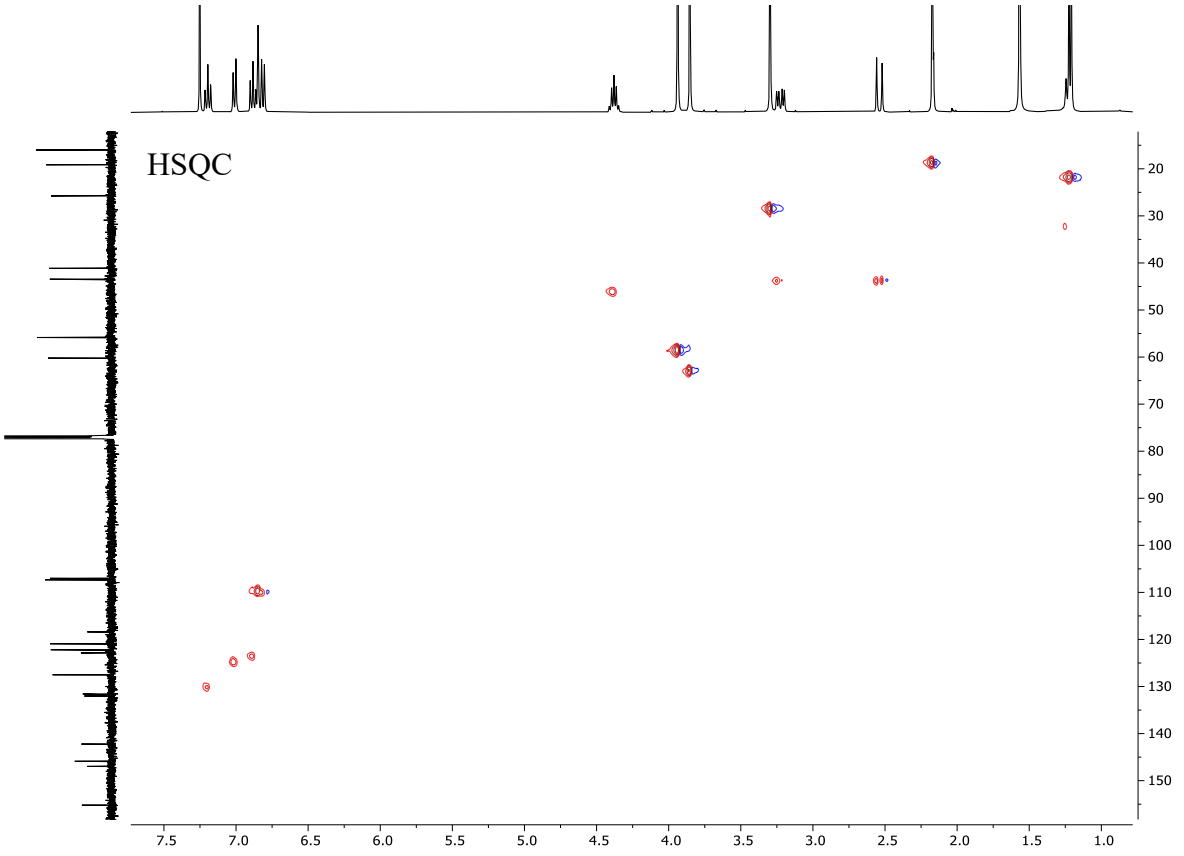
HSQC
20
30
40
50
60
70
80
90
100
110
120
130
140
150
7.5
7.0
6.5
6.0
5.5
5.0
4.5
4.0
3.5
3.0
2.5
2.0
1.5
1.0

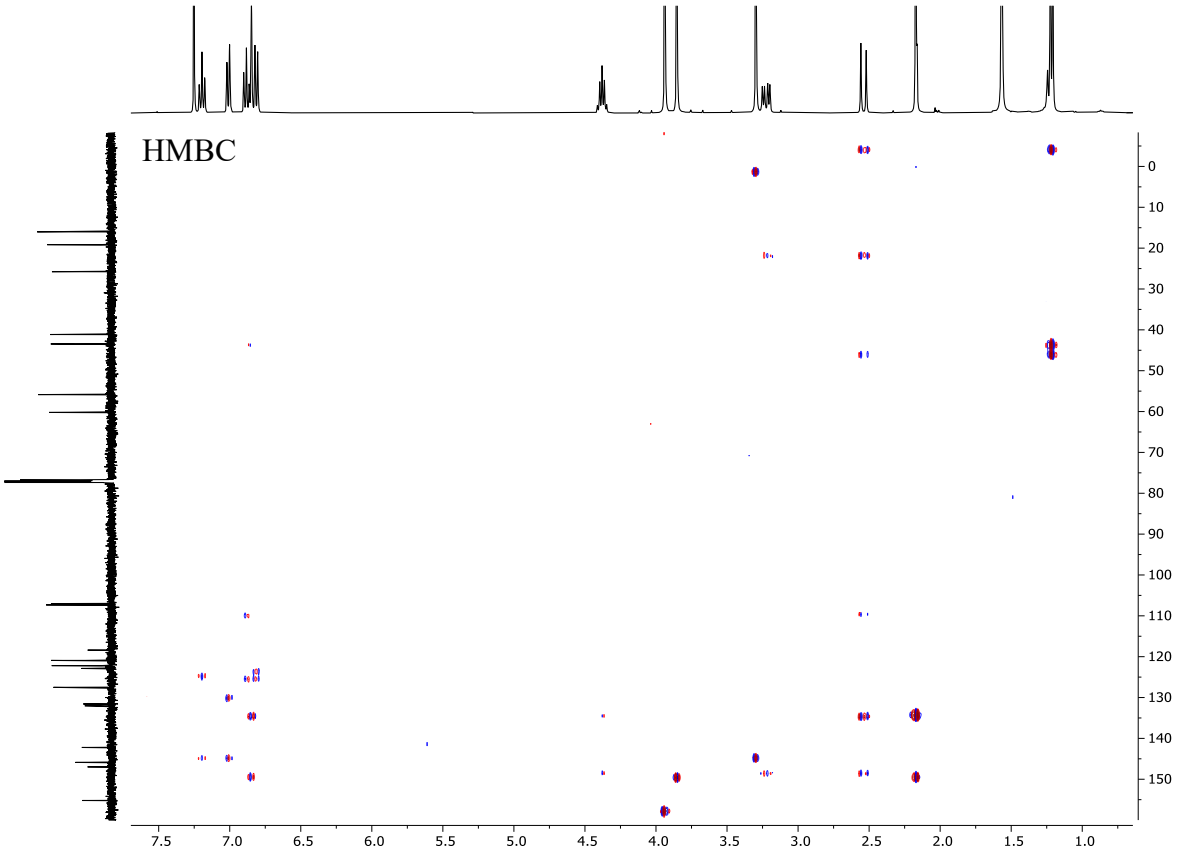
HMBC
0
10
20
30
40
50
60
70
80
90
100
110
120
130
140
150
7.5
7.0
6.5
6.0
5.5
5.0
4.5
4.0
3.5
3.0
2.5
2.0
1.5
1.0

(*Z*)-3-(5,6-dimethoxy-2,7-dimethyl-2,3-dihydro-1H-inden-1-ylidene)-1-methylindolin-2-one (*Z*s-1) ($CDCl_3$)

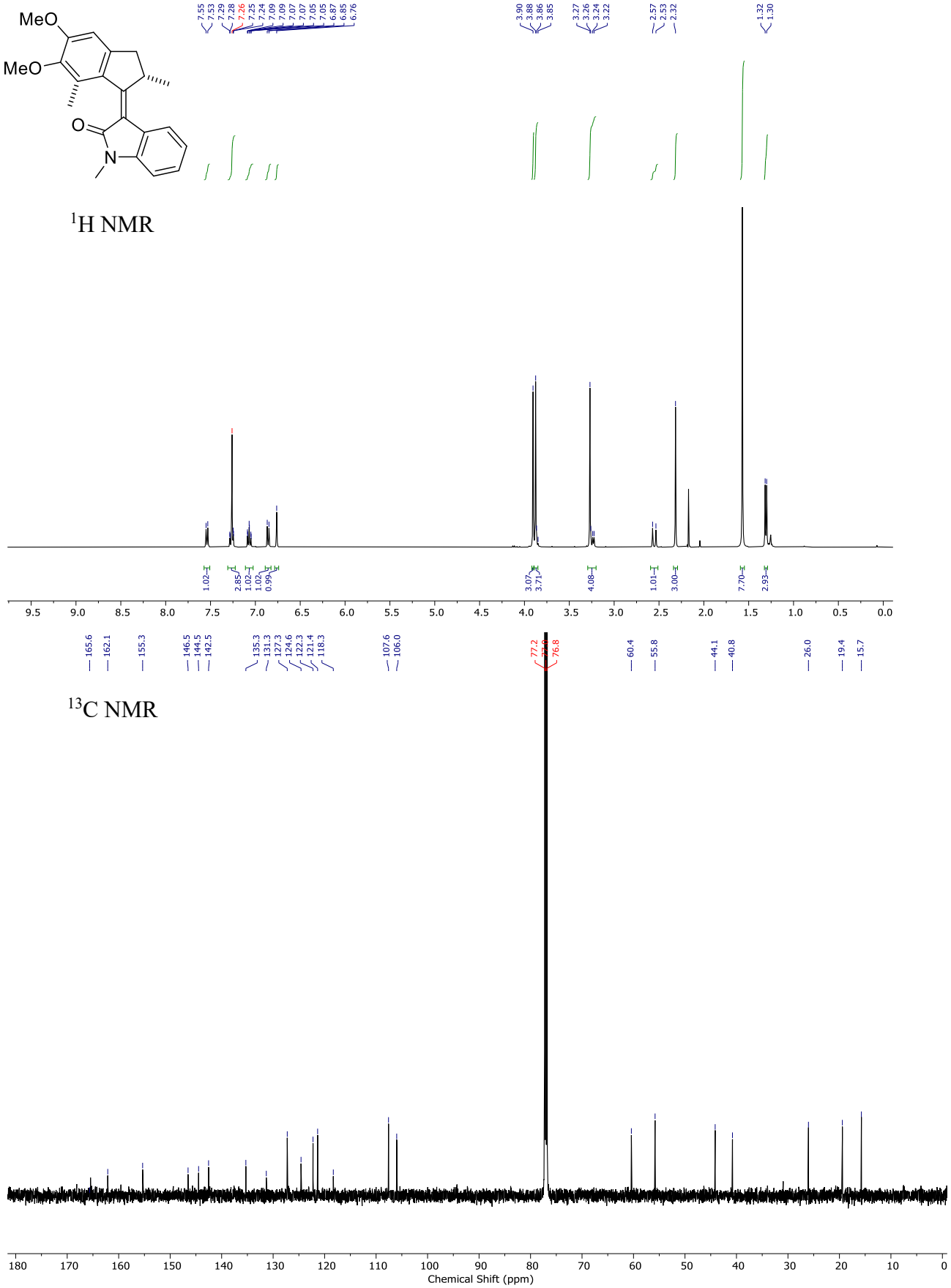

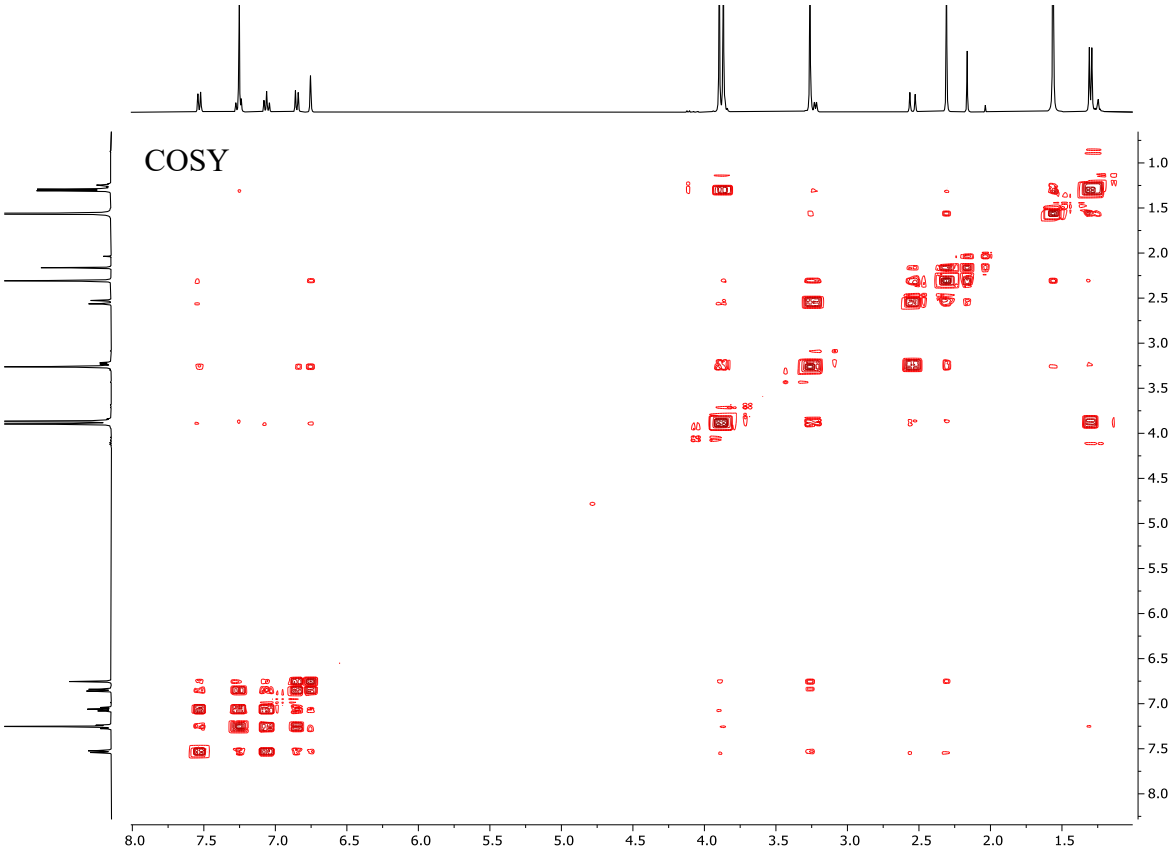
COSY
8.0
7.5
7.0
6.5
6.0
5.5
5.0
4.5
4.0
3.5
3.0
2.5
2.0
1.5
1.0

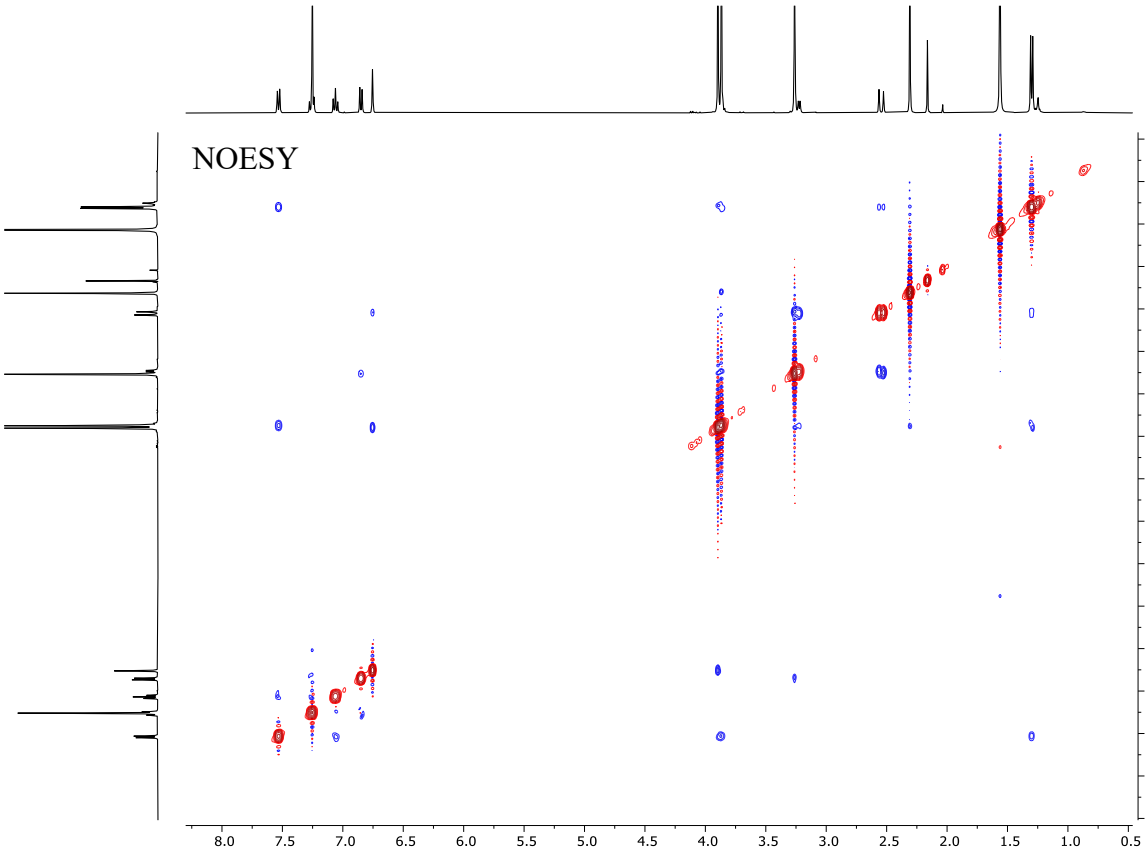
NOESY
8.0
7.5
7.0
6.5
6.0
5.5
5.0
4.5
4.0
3.5
3.0
2.5
2.0
1.5
1.0
0.5

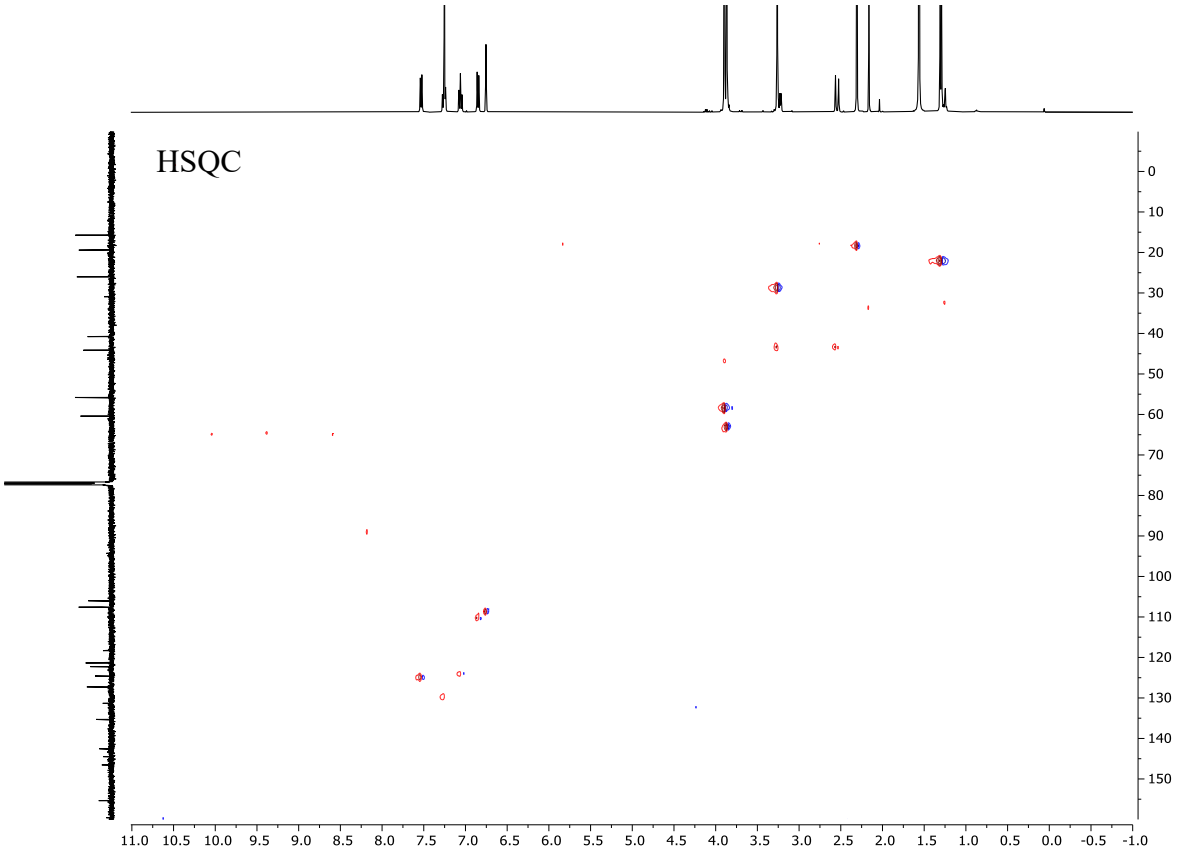
HSQC
0
10
20
30
40
50
60
70
80
90
100
110
120
130
140
150
11.0 10.5 10.0 9.5 9.0 8.5 8.0 7.5 7.0 6.5 6.0 5.5 5.0 4.5 4.0 3.5 3.0 2.5 2.0 1.5 1.0 0.5 0.0 -0.5 -1.0

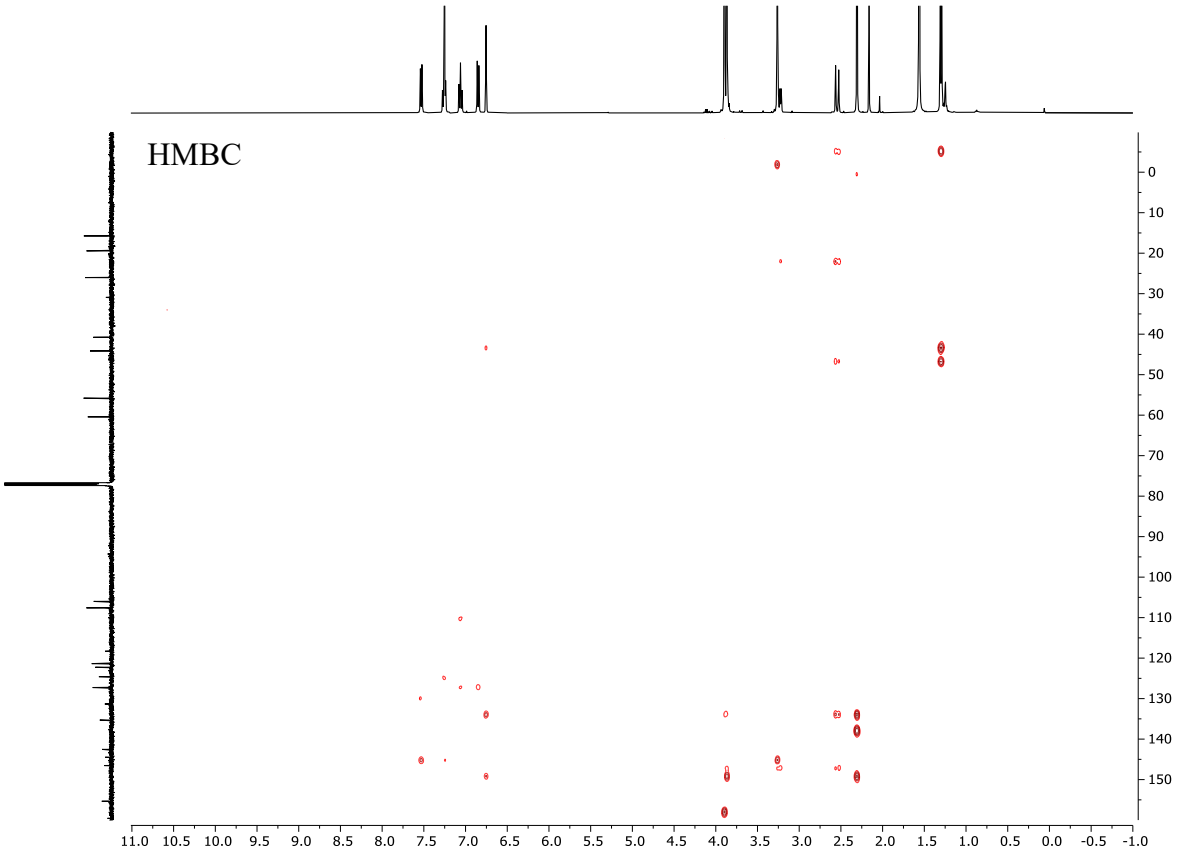
HMBC
0
10
20
30
40
50
60
70
80
90
100
110
120
130
140
150
11.0 10.5 10.0 9.5 9.0 8.5 8.0 7.5 7.0 6.5 6.0 5.5 5.0 4.5 4.0 3.5 3.0 2.5 2.0 1.5 1.0 0.5 0.0 -0.5 -1.0

3. NMR studies of the rotation cycle

A 3.8 × 10^{-3} M solution of motor ***E*S-1** in CD_2Cl_2 was prepared and transferred into an NMR tube which was subsequently fitted with a glass optic fibre for *in situ* irradiation studies. The sample was place in a Varian Unity Plus 500 MHz NMR and cooled to –90 °C. ^{1}H NMR spectra were recorded while irradiating ***E*S-1** at –90 °C with a 365 nm LED, forming ***Z*M-1**. Switching off the irradiation but keeping the temperature constant allowed to prove that the thermal helix inversion and formation of ***Z*S-1** occurs at low temperature, competing with the photochemical formation of ***Z*M-1**. Irradiation of the stable *Z*-isomer which is present at –90 °C leads to ***E*M-1**. Switching the irradiation back on at –90 °C yields the PSS and finally switching off the irradiation and raising the temperature at –45 °C allows to obtain the PSS observed by UV/Vis spectroscopy (see Figure 2D). All four species associated to the rotation cycle, namely ***E*S-1**, ***Z*M-1**, ***Z*S-1** and ***E*M-1**, could be observed in these conditions, confirming the unidirectionality of the rotation.

To confirm the unidirectionality of the motor we also irradiated ***Z*S-1** at low temperature. In this case, irradiation at –90 °C forms only ***E*M-1**. The unimolecular event is confirmed comparing the kinetics of depletion and of ***Z*S-1** and formation of ***E*M-1**, ruling out the possibility of a photochemical helix inversion.

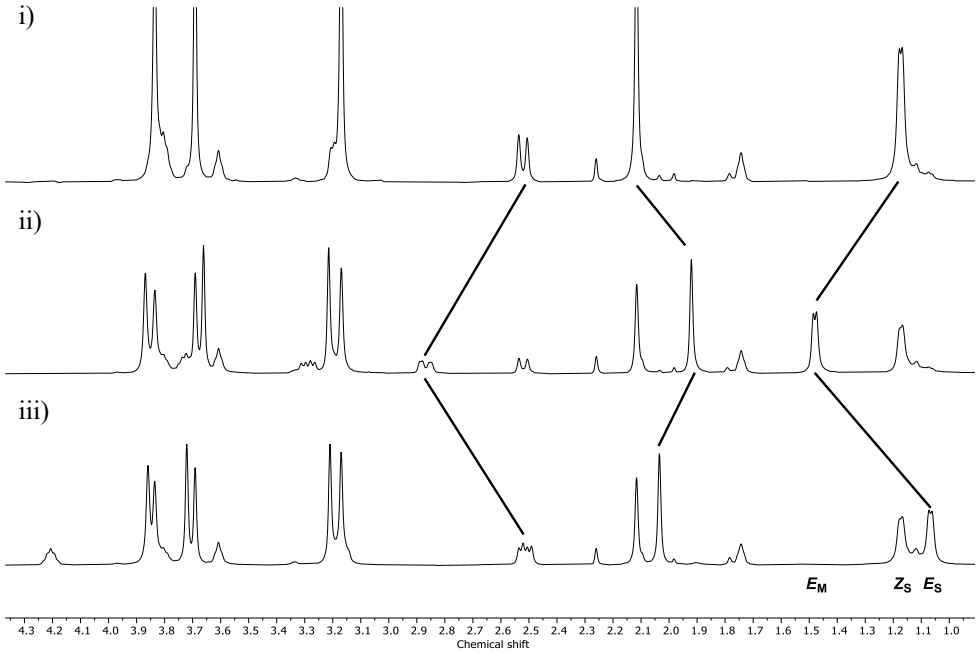

Figure S2. ^{1}H NMR irradiation studies of motor **1** in its Z_S form in CD_2Cl_2 (c = 3.0 · 10^{-3} M). i) Stable ***Z*S-1** before irradiation; ii) after 60 min irradiation at 365 nm at –90 °C; iii) no irradiation, THI, –45 °C, 15 min.

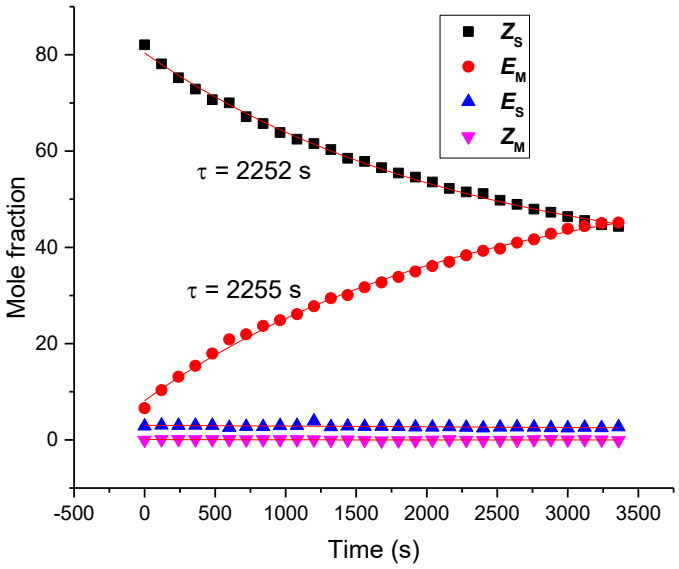

Figure S3. Kinetic of the initial irradiation of Stable ***Z*s-1.**

4. Separation of enantiomers and CD spectroscopy

The irradiation could be also repeated on the enantiomerically pure compounds. CD spectroscopy confirmed the absence of racemization during the irradiation process (*vide infra*). Prior to the separation of the enantiomers of each stable species, the *E*/*Z* isomers of **1** were separated by HPLC on a Grace Alltima HP silica column (150 mm * 3 mm, 3 µm particle size). Enantiomers of ***E*s-1** and ***Z*s-1** were separated on a Daicel CHIRALPAK OD-H analytical column (250 mm × 4.6 mm, 5 µm particle size).

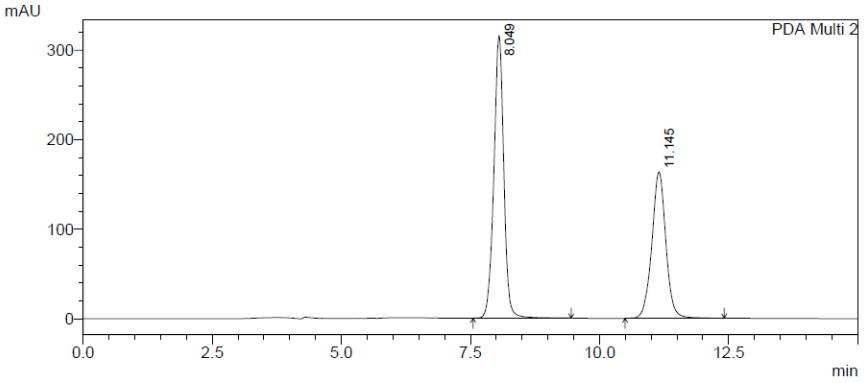

Figure S4. HPLC trace of the PSS of ***E*s-1**/***Z*s-1** (obtained irradiating the sample with a 400 nm LED) monitored at 364 nm. Conditions: Heptane/Propan-2-ol 95:5, 0.5 mL min^{-1}, 40 °C. t_R^1 = 8.05 min (*E*-1); t_R^2 = 11.14 min (*Z*-1).

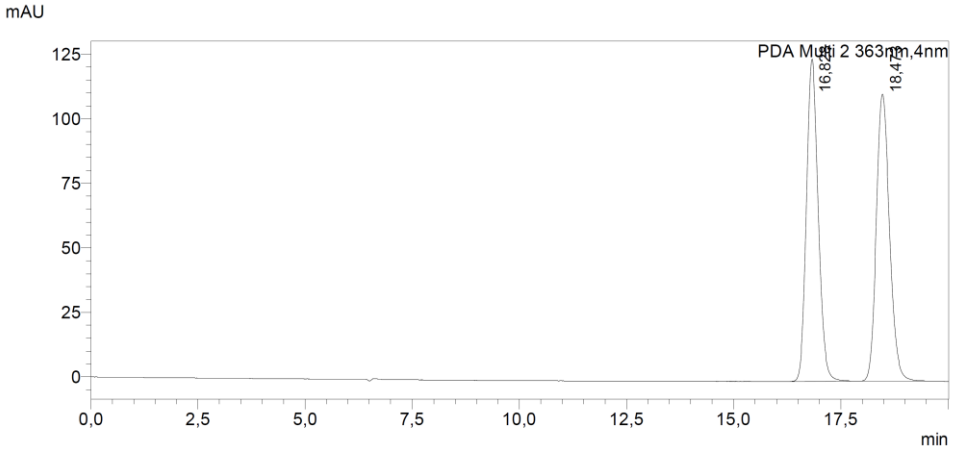

Figure S5. Screening run for the separation of the enantiomers of ***E*s-1**. Conditions: Heptane/Propan-2-ol 95:5, 0.5 ml/min, 40 °C ; t_R^1 = 16.83 min, t_R^2 = 18.47 min.

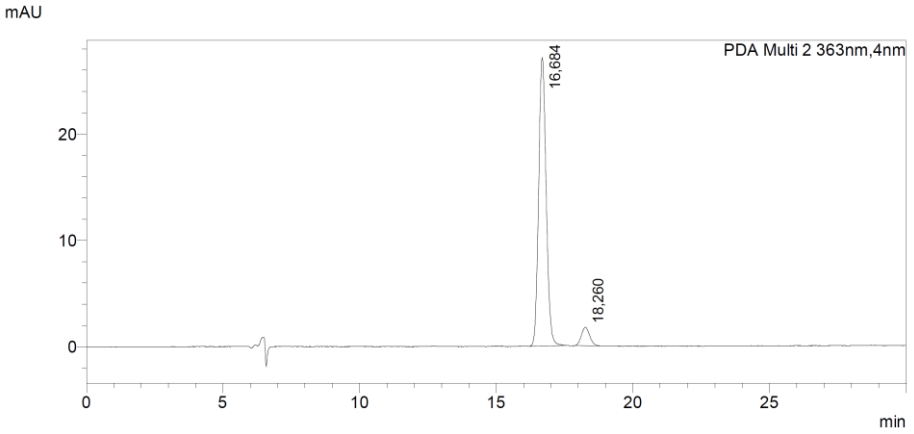

Figure S6. *E*S-1 fraction 1; *e.r.*: 93.3/7.7

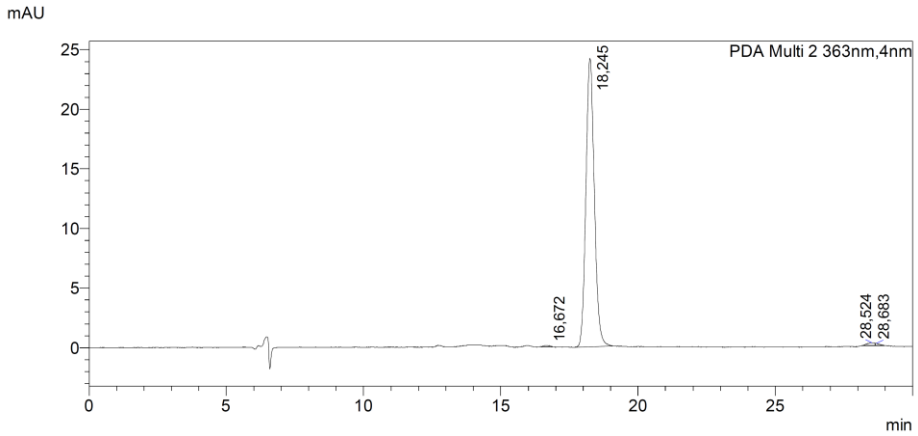

Figure S7. *E*S-1 fraction 2; *e.r.*: 99.7/0.3

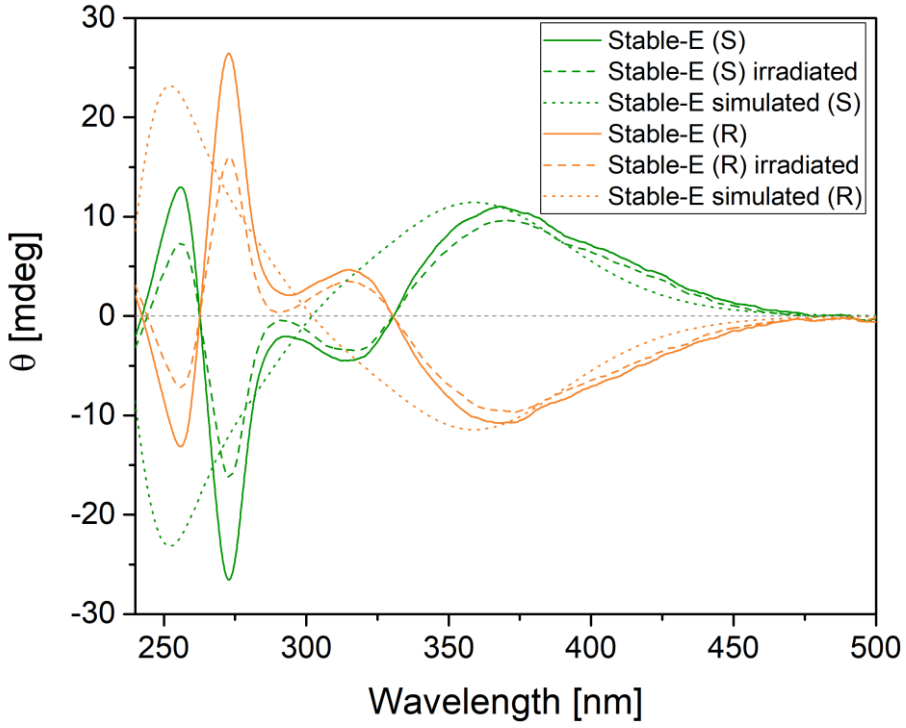

Figure S8. Experimental and simulated CD spectra of (S) and (R) stable ***E*S-1**, before and after irradiation with a 400 nm LED. Irradiation was maintained until no further changes in the CD signal were detected. The assignment of the stereochemistry of the compounds was confirmed comparing the experimental and predicted at the TD(25 states)-ωB97X-D/6-311+G(2d,p)//MP2/6-31G(d) level in methanol (PCM).

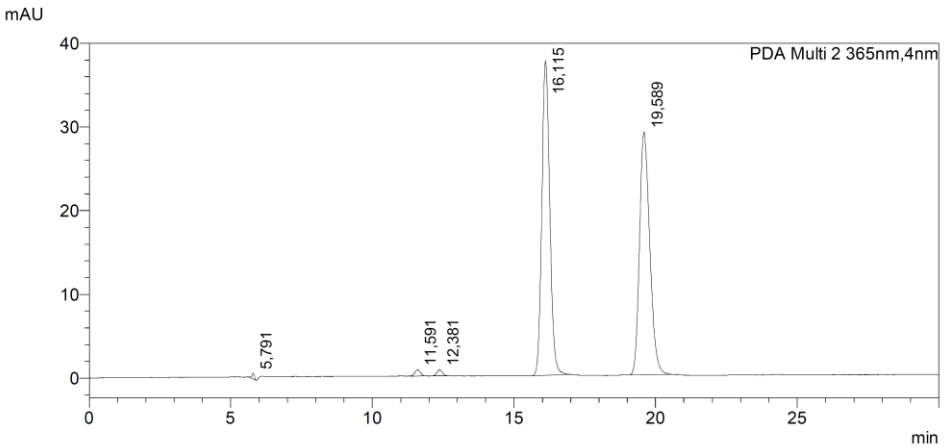

Figure S9. Screening run for the separation of the enantiomers of ***Z*S-1**. Conditions: Heptane/Propan-2-ol 90:10, 0.5 ml/min, 40 °C ; t_R^1 = 16.11 min, t_R^2 = 19.59 min.

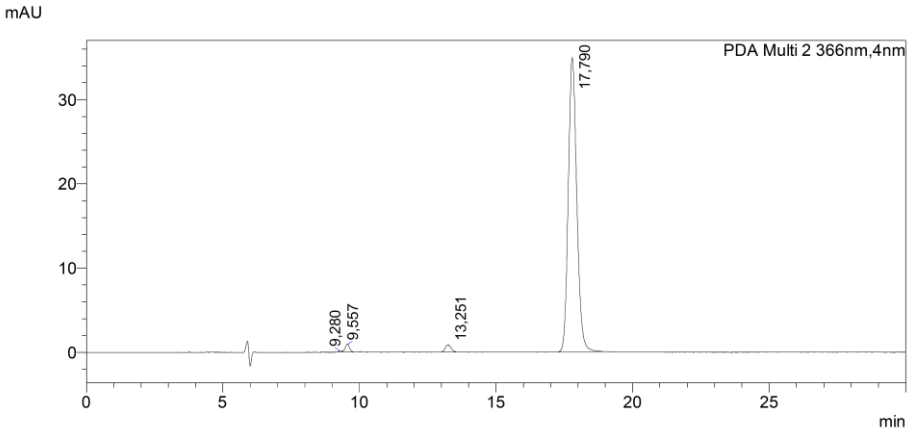

Figure S10. *Z*S-1 fraction 1; *e.r.*: No other enantiomer detected (note: discrepencies in the retention time are due to the use of a different HPLC machine).

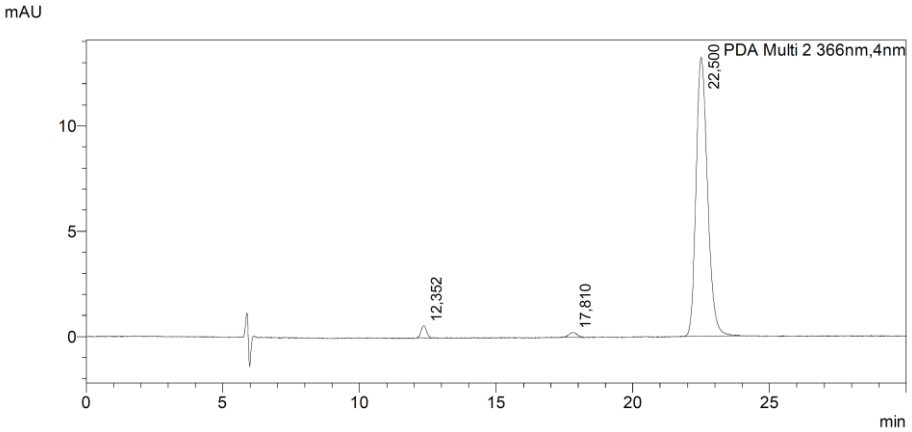

Figure S11. *Z*S-1 fraction 1; *e.r.*: 98.8/1.2 (note: discrepencies in the retention time are due to the use of a different HPLC machine).

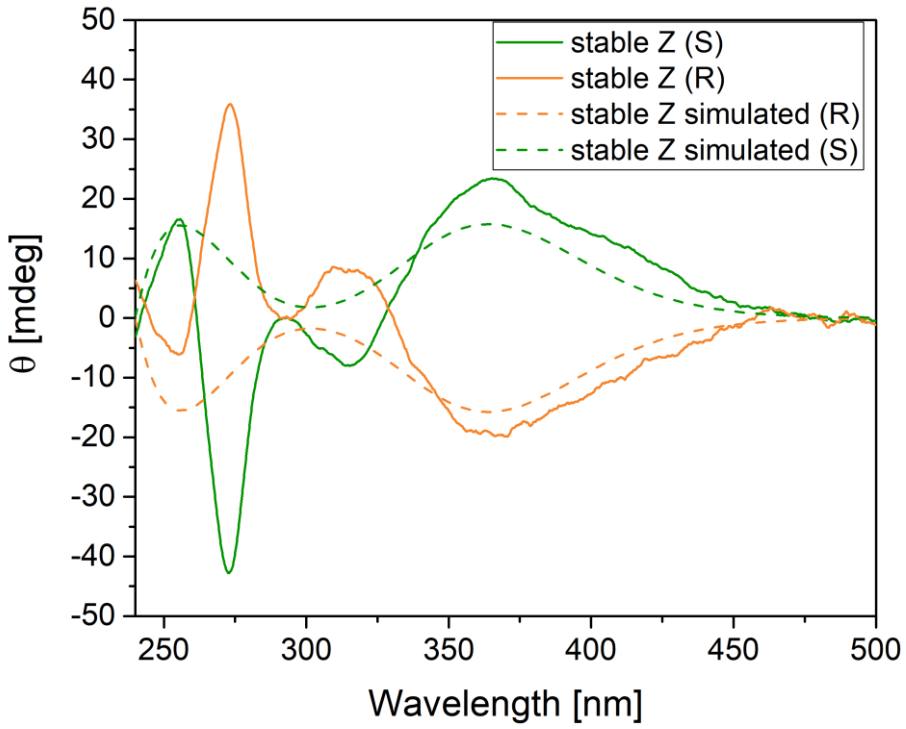

Figure S12. Experimental and simulated CD spectra of (S) and (R) ***Z*s-1**, before and after irradiation with a 400 nm LED. The assignment of the stereochemistry of the compounds was confirmed comparing the experimental and predicted at the TD(25 states)-ωB97X-D/6-311+G(2d,p)//MP2/6-31G(d) level in methanol (PCM).

5. X-Ray of *E*s-1

A single-crystal of ***E*s-1** was mounted on a cryoloop and placed in the nitrogen stream (100 K) of a Bruker-AXS D8 Venture diffractometer. Data collection and processing was carried out using the Bruker APEX3 software suite.[2] A multi-scan absorption correction was applied, based on the intensities of symmetry-related reflections measured at different angular settings (*SADABS*).[3] The structure was solved using *SHELXT*[4] and refinement was performed using *SHELXL*.[5] The hydrogen atoms were generated by geometrical considerations, constrained by idealized geometries and allowed to ride on their carrier atoms with an isotropic displacement parameter related to the equivalent displacement parameter of their carrier atoms. No A- or B-level alerts were raised by CheckCIF for the fully refined structure. Distance measurements were performed using PLATON.[6]

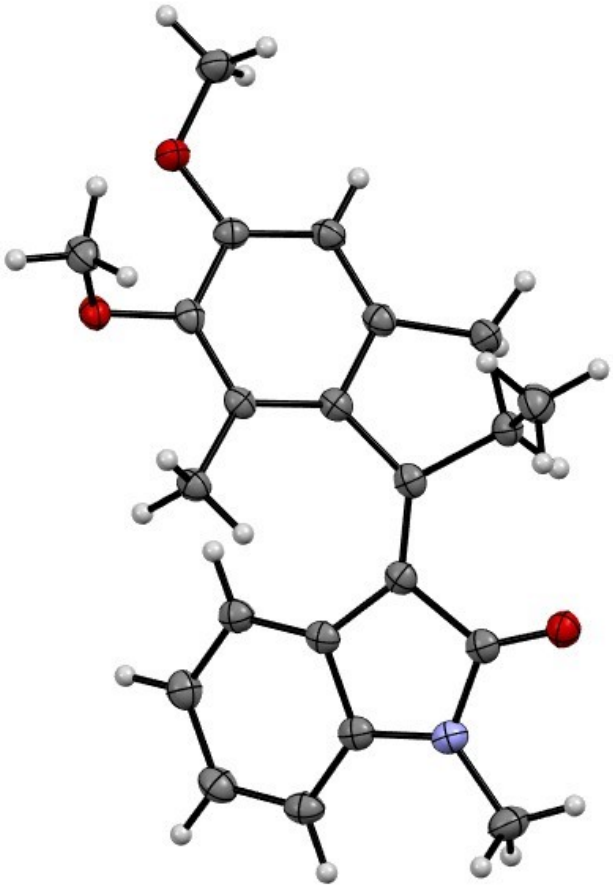

Figure S13. ORTEP image (ellipsoid at 50% probability) of ***E*s-1**.

Nr.	LP-18071
Name	Es-1
Formula	C_{22} H_{23} N_1 O_3
Molecular Weight	349.41
Crystal System	orthorhombic
T [K]	100(2)
Space Group	*P b c a*
a [Å]	17.9980(5)
b [Å]	9.6252(2)
c [Å]	20.8083(5)
α [°]	90
β [°]	90
γ [°]	90
V [Å^3]	3604.71(15)
Z	8
D_{calc} [g·cm^{-3}]	1.288
F(0 0 0)	1488
h_{min}, h_{max}	–22, 23
k_{min}, k_{max}	–12, 11
l_{min}, l_{max}	–26, 26
μ [mm^{-1}]	0.683
Crystal Size [mm]	0.12 x 0.10 x 0.04
Colour, Shape	block
R_{int}	clear_light_yellow
$θ_{min}$, $θ_{max}$ [°]	4.249, 80.240
Total Reflections (before merge)	80118
Data (I>3 x sigma(I)) [Reflections,Parameters,Restraints]	3928, 240, 0
S (=GooF)	1.031
Min. Residual Density [e/Å^3]	-0.204
Max. Residual Density [e/Å^3]	0.231
Threshold Expression	I>2sigma(I)
R_1	0.0518
wR_2	0.1005

6. UV/vis spectra and Quantum Yield Determination

Steady state photochemistry

For a typical experiment, a stirred solution (2 mL) of a compound (c ~ 40 μM) in methanol was irradiated from the side in a fluorescence quartz cuvette (width = 1.0 cm) using a custom-built (Prizmatix/Mountain Photonics) multi-wavelength fiber coupled LED-system (FC6-LED-WL) using the 365A or 390B LEDs with FWHM ≤ 20 nm. The setup is described in more details elsewhere.[7] For all kinetic and quantum yield experiments, the temperature was maintained at 293K using a Quantum Northwest TC1 temperature controller. Electronic absorption spectra were measured using an Agilent 8453 at intervals of 0.5 s. Raw data was processed using Agilent UV-Vis ChemStation B.02.01 SP1, Spectragryph 1.2 and Origin 2018.

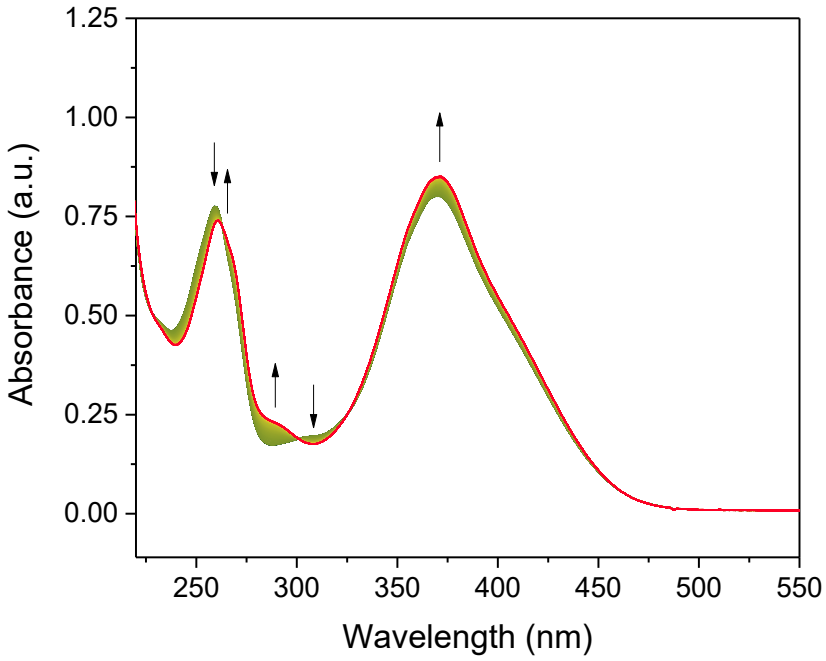

Figure S14. Time resolved UV-Vis irradiation (200 s) of a solution in methanol of ***E*S-1** (3.8×10^{-5} M, in green) with a 390 nm LED showing the spectral changes upon formation of the photostationary state (in red).

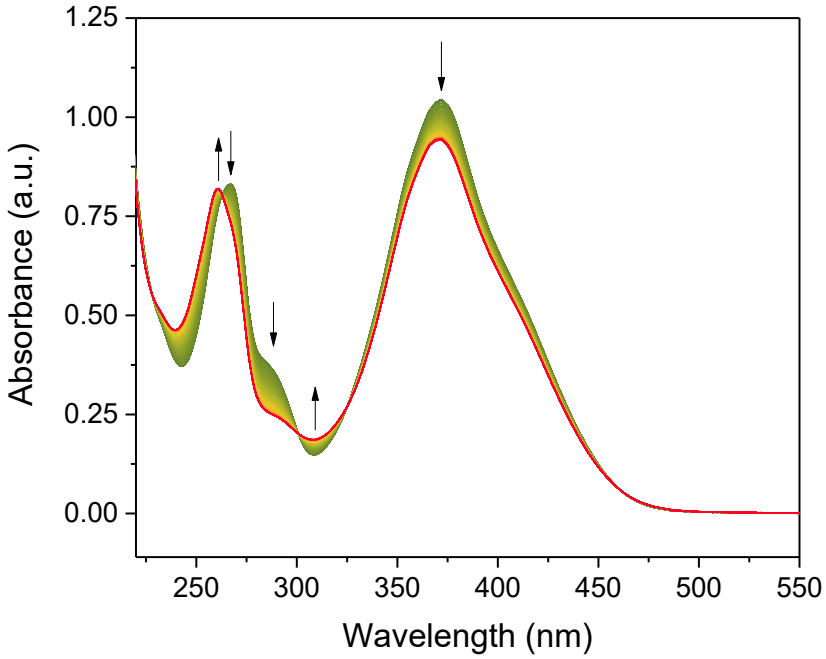

Figure S15. Time resolved UV-Vis irradiation (200 s) of a solution in methanol of ***Z*s-1** (4.1×10^{-5} M, in green) with a 390 nm LED showing the spectral changes upon formation of the photostationary state (in red).

Chemical actinometry

A modification of a standard protocol was applied for the determination of the photon flux.[8,9] An aqueous H_2SO_4 solution (0.05 M) containing freshly recrystallized $K_3[Fe(C_2O_4)_3]$ (41 mM, 2 mL, 1 cm quartz cuvette) was irradiated at 20 °C for a given period of time in the dark with a 365 nm LED. The solution was then diluted with 1.0 mL of an aqueous H_2SO_4 solution (0.5 M) containing phenanthroline (1 g/L) and NaOAc (122.5 g/L) and left to react for 10 min. The absorption at λ= 510 nm was measured and compared to an identically prepared non-irradiated sample. The concentration of $[Fe(phenanthroline)_3]^{2+}$ complex was calculated using its molar absorptivity (ε = 11100 M^{-1} cm^{-1}) and considering the dilution. The quantity of Fe^{2+} ions expressed in mol was plotted versus time (expressed in seconds, s) and the slope, obtained by linear fitting the data points to the equation y = ax + b, equals the rate of formation of the Fe^{2+} ion at the given wavelength. This rate can be converted into the photon flux (I) by dividing it by the quantum yield of $[Fe(phenanthroline)_3]^{2+}$ complex at 365 nm (Φ^{365nm} = 1.21)[10] and by the probability of photon absorption at 365 nm of the Fe^{3+} complex (approximated to 1 as we were working in the total absorption regime). The obtained photon flux was $I = 4.21\cdot10^{-5}$ mE s^{-1}.

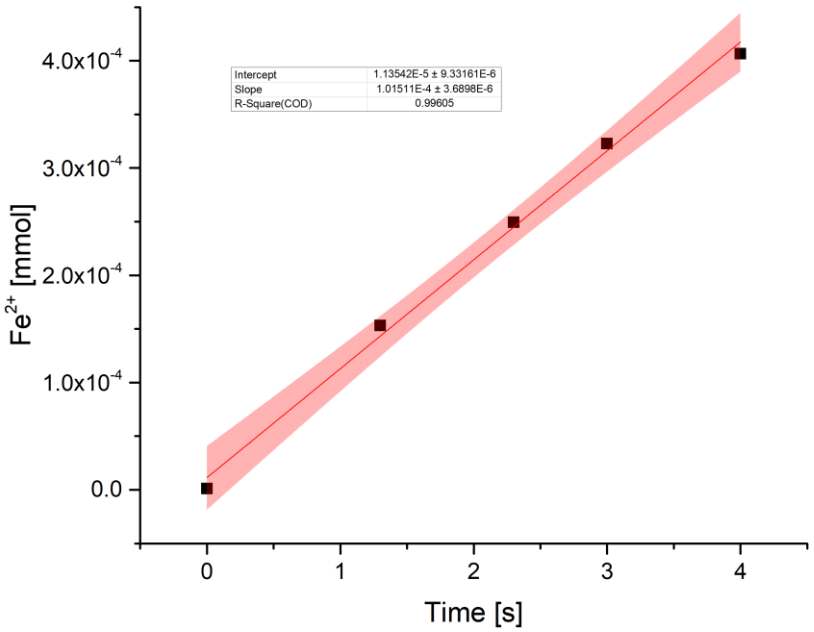

Figure S16. Linear fitting of the Fe^{2+} moles generated upon irradiation at different irradiation times with the associated confidence interval (95%). The fitting afforded a photon flux I = $4.21 \cdot 10^{-5}$ mE·s^{-1}.

Quantum Yield determination

Obtaining a direct measure of the quantum yield of isomerization for motor **1** is an intrinsically challenging process. Indeed, the THI barriers are prohibitive when it comes to measure the isomerization quantum yield between a stable state and a metastable state, because the population of the metastable state at room temperature is risible. Considering this feature, we can measure two approximated quantum yields (a forward, QY_{EZ}, and a backward one, QY_{ZE}) directly connecting ***E*s-1** and ***Z*s-1**, neglecting the contribution of the metastable states, having consequently:

$$\boldsymbol{E}\text{s-1} \underset{QY_{ZE}}{\overset{QY_{EZ}}{\rightleftharpoons}} \boldsymbol{Z}\text{s-1}$$

To do so, solutions of ***E*s-1** and ***Z*s-1** in methanol (40 μM) spectra were irradiated with a 365 nm LED and the spectra were collected over the first ca. 200 s of irradiation, following the evolution of the absorption maximum; baseline corrections were carried out to correct for baseline drifting, after which the data was processed in QYMain (which can be downloaded from https://www.nature.com/articles/srep41145#Sec14) developed by Stranius & Börjesson.[8] Eq. 14 in the original article

$$\frac{d[A]}{dt} = -\frac{QY_{EZ} \cdot I \cdot \beta_E(t)}{N_A \cdot V} + \frac{QY_{ZE} \cdot I \cdot \beta_Z(t)}{N_A \cdot V}$$

was used to determine both approximated QYs. I is the photon flux, previously determined with ferrioxalate actinometry, N_A the Avogadro number, V the total volume of the irradiated solution (2 mL) and β the fractions of photons absorbed by either ***E*s-1** or ***Z*s-1**. 20763 $M^{-1} \cdot cm^{-1}$ and 24536 M^{-}

^{1}·cm^{-1} were used as the molar extinction coefficients for ***E*s-1** and ***Z*s-1** at the irradiation wavelength (ca. corresponding to the absorption maximum). Following the isomerization of ***E*s-1** we obtained a value for QY_{EZ} = 0.081 and QY_{ZE} = 0.112. Following the isomerization of ***Z*s-1** gave QY_{EZ} = 0.095 and QY_{ZE} = 0.129. As an average, this method provided QY_{EZ} = 0.088 and QY_{ZE} = 0.120.

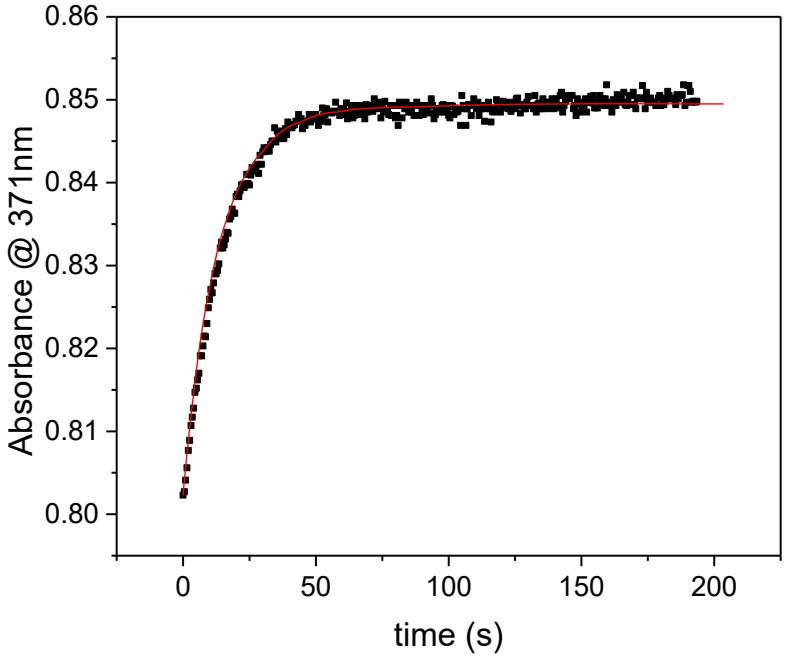

Figure S17. Evolution of the absorption at 371 nm during the irradiation of ***E*s-1** with a 365 nm LED. The red line represents the fit as exported from the QYMain program.

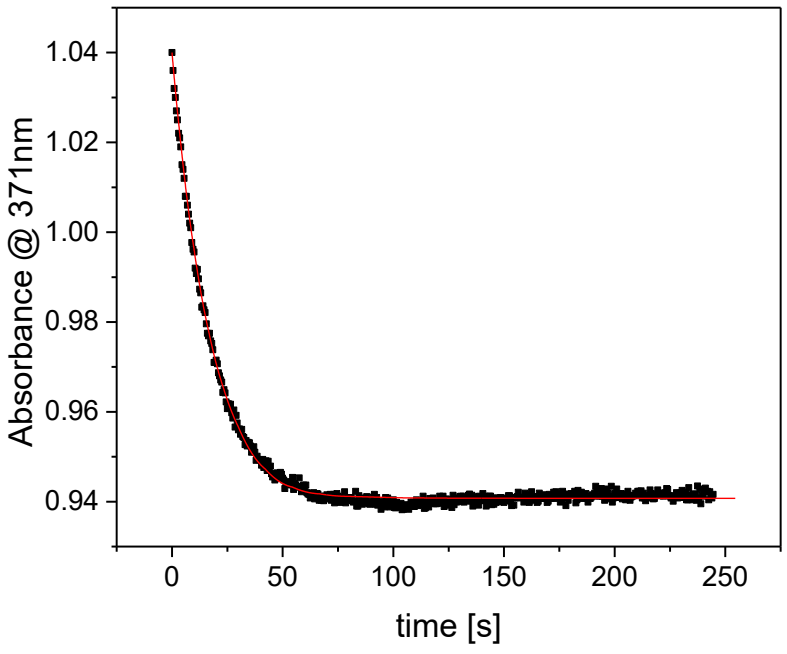

Figure S18. Evolution of the absorption at 371 nm during the irradiation of ***Z*s-1** with a 365 nm LED. The red line represents the fit as exported from the QYMain program.

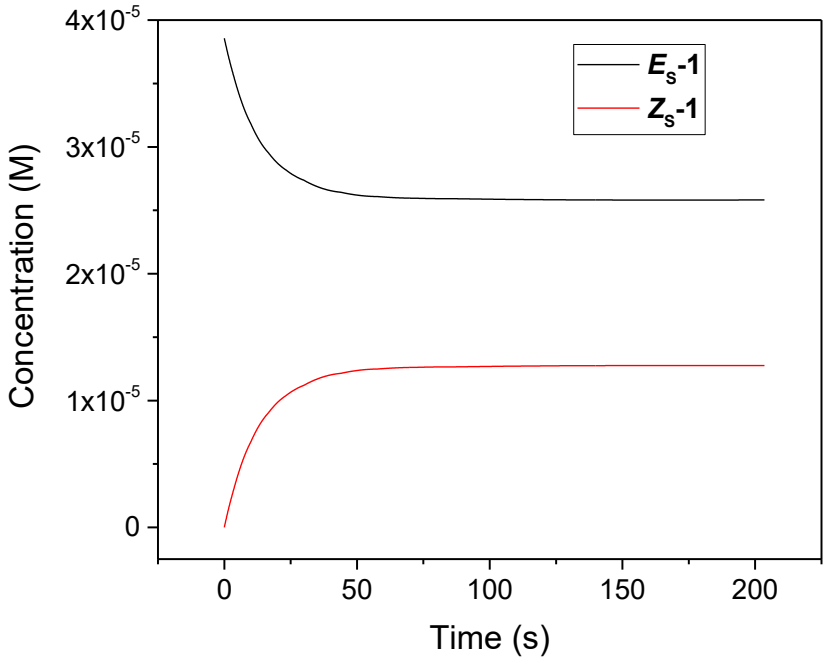

Figure S19. Evolution of the concentration of ***E*S-1** and ***Z*S-1** during the irradiation of ***E*S-1** with a 365 nm LED as fitted by the QYMain program.

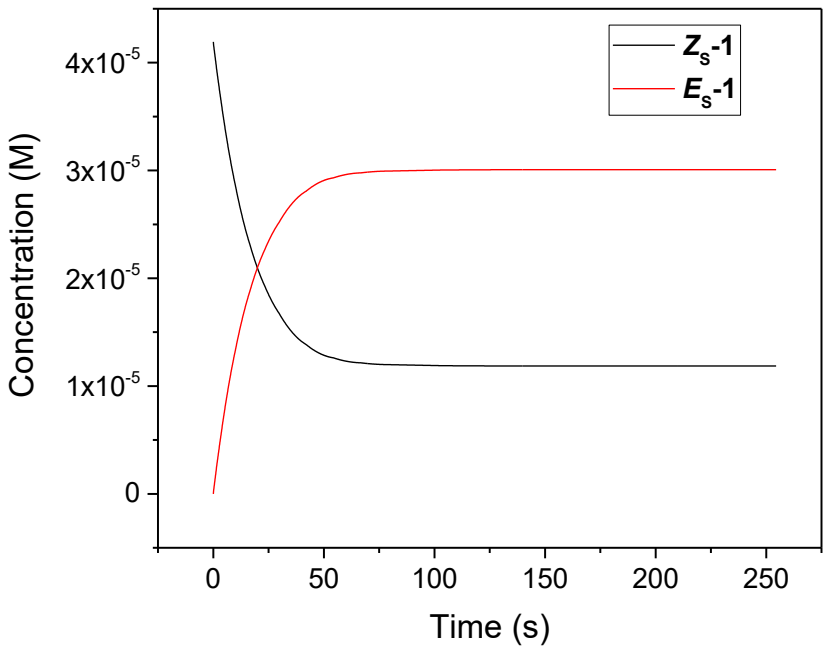

Figure S20. Evolution of the concentration of ***E*S-1** and ***Z*S-1** during the irradiation of ***Z*S-1** with a 365 nm LED as fitted by the QYMain program.

The isomerization of ***E*s-1** was also followed in its initial stages with HPLC analysis (Grace Alltima HP silica column (150 mm · 3 mm, 3 µm particle size)). In this way, QY_{EZ} can be derived, using the initial slope method[11] upon irradiation in total absorption regime conditions.[8] Due to the higher concentrations used in this measurement, we can approximate the photochemical conversion of ***E*s-1** to ***Z*s-1** with a linear fit that fulfills the following equation:[8]

$$[E] = [E_{t0}] - \frac{QY_{EZ} \cdot I}{N_A \cdot V} \cdot t$$

with [E] the concentration of ***E*s-1** at time *t* and $[E_{t0}]$ the initial concentration of the sample.

The measure was triplicated, obtaining $QY_{EZ} = 0.075 \pm 0.003$

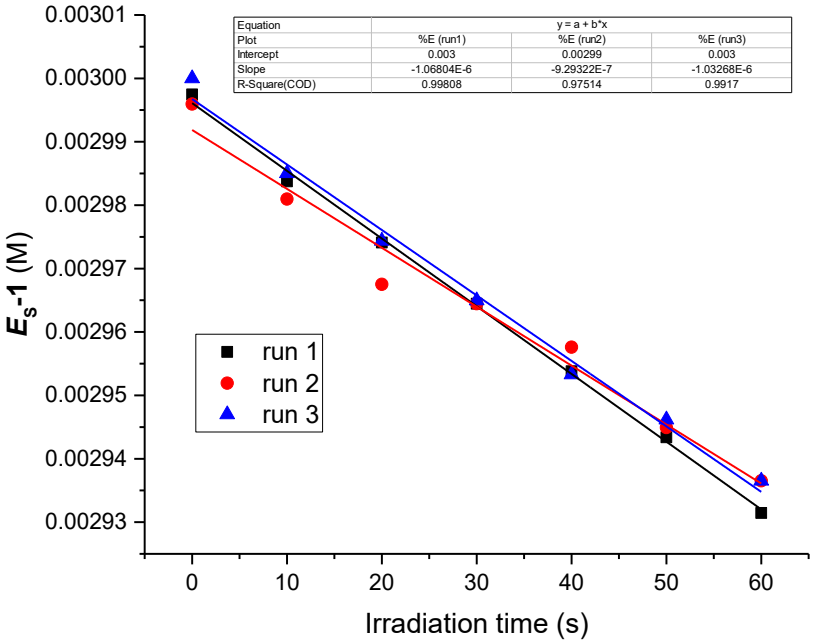

Figure S21. Evolution of the concentration of ***E*s-1** (0.003M solution in methanol) upon irradiation with a 365 nm LED. The concentration was detected with a HPLC - Grace Alltima HP silica column (150 mm * 3 mm, 3 µm particle size).

7. Eyring analysis

NMR samples in d_4-methanol (ca. $1 \cdot 10^{-3}$ M) were irradiated with a Thorlabs LED (M395F1) between −45 and −92.5 °C to reach PSS. The thermal helix inversion was followed plotting the decay of the integrals of ***E*M-1** and ***Z*M-1** after switching off the irradiation, in order to extract the rate constants used for the Eyring plots. A least squares analysis was performed on the Eyring equation to retrieve the $\Delta G^{\ddagger}$ of THI.

The Eyring analysis provided the activation values reported in Table S1.

Table S1. Activation parameters for the THI isomerization reactions of motor **1.**

	$\Delta G^{\ddagger}$	**$\Delta H^{\ddagger}$**	**$\Delta S^{\ddagger}$**
	Kcal·mol^{-1}	Kcal·mol^{-1}	cal·K^{-1}·mol^{-1}
***Z*M-1 → *Z*S-1**	11.8 ± 0.8	15.0	10.8
***E*M-1 → *E*S-1**	17.4 ± 0.7	9.4	−27.2

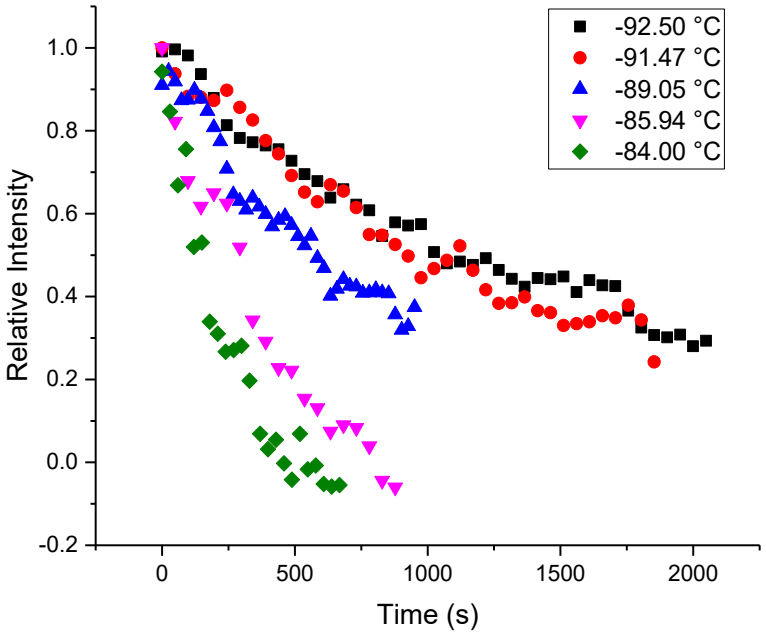

Figure S22. Integration of the signal at 1.45 ppm assigned as the methyl at the stereogenic centre of ***Z*M-1** (in d_4-methanol) generated upom irradiation of ***E*S-1** in methanol, after the 365 nm LED was switched off. The temperature of the NMR probe was measured measuring the relative distance between the solvent residual signals.

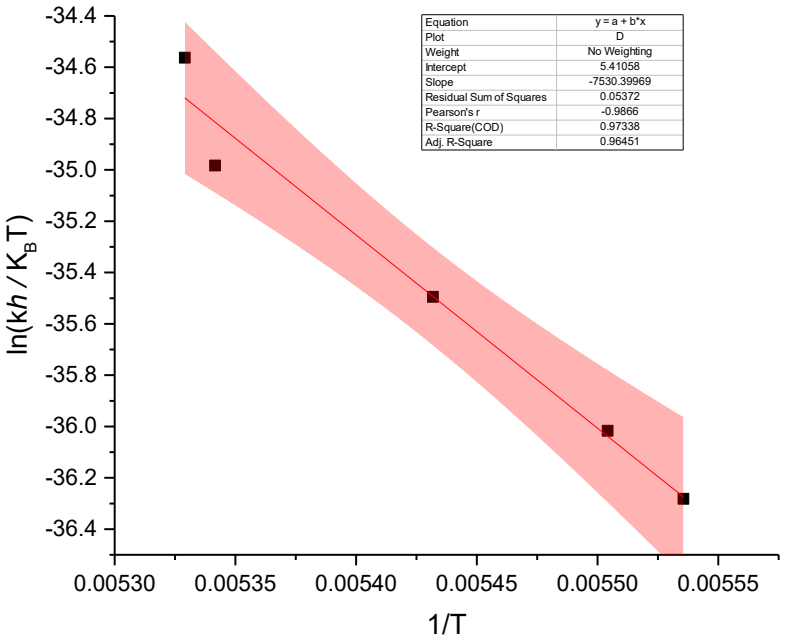

Figure S23. Eyring plot analysis of thermal isomerization step from ***Z*M-1** to ***Z*S-1** in d_4-methanol. Thermodynamic parameters of the transition state were obtained by fitting the linearized form of the Eyring equation. The red band indicates the 95% confidence interval.

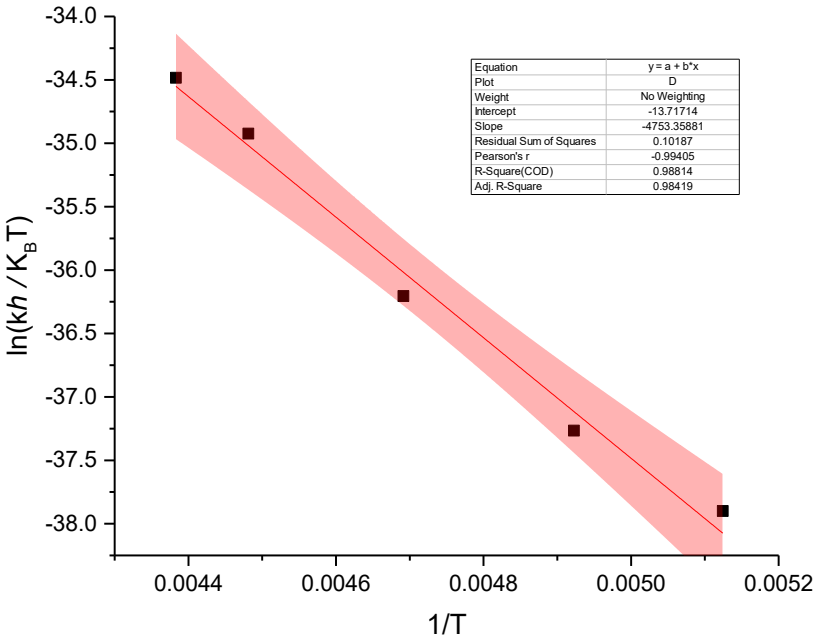

Figure S24. Eyring plot analysis of thermal isomerization step from ***E*M-1** to ***E*S-1** in d_4-methanol. Thermodynamic parameters of the transition state were obtained by fitting the linearized form of the Eyring equation. The red band indicates the 95% confidence interval.

8. Transient Absorption Spectroscopy

8.1. Methods

Methanol solutions of *E* and *Z* stable isomers of compound **1** were prepared to an absorbance A=1/mm, at their absorption maximum of λmax =370 nm (***E*s-1**), 371 nm (***Z*s-1**), see Figure 2.A. Stable ***E*s-1** was also dissolved in hexane (λmax = 361 nm, see Figure S27.A) to monitor the influence of the solvent polarity on the photoreaction dynamics. These samples were investigated by femtosecond transient absorption (TA) spectroscopy with an experimental set-up described elsewhere,[12,13] using a pump pulse at 400 nm and a white-light probe pulse offering an absorption detection window spanning from 300 nm to 750 nm. The time resolution is in the range 60 fs (400nm pulse) to 80 fs (330 nm pulse). The samples were circulated in a 0.5-mm thick cuvette with a peristaltic pump. The raw data are processed to subtract the solvent signal (recorded separately) and to correct for the chirp of the probe – i.e. probe-wavelength-dependence of time zero (see the Supplementary Information of [12] for details).

8.2. TA data

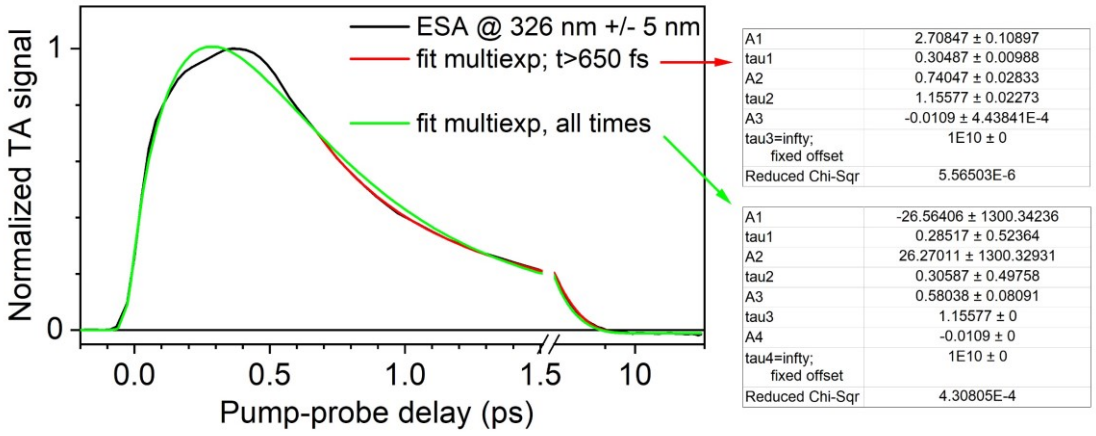

Figure S25. Illustration of the failure of the multiexponential fit of the ESA decay kinetics observed at 326 nm for compound ***Z*s-1** (main text, Figure 4, bottom). In red, we fit only the tail of the decay (time delays larger than ~650 fs) with a biexponential fit (tau1, tau2 and their corresponding amplitudes A1, A2) with on additional offset (i.e. infinite time constant, with negative amplitude A3). The fit is very good, with reduced $\chi^2 \sim 5.10^{-6}$. In green we fit the entire kinetic trace. The fit is particularly bad in the range 0.1 to 0.6 ps (i.e. large residuals) with a reduced χ^2 increased by as much as two orders of magnitude. The fit hardly converges to the near cancellation of two exponential contributions with nearly identical, sub-ps time constants (tau1 and tau2) and unphysically large and opposite amplitudes (A1 and A2). No reliable time scale, nor average excited state lifetime, nor any underlying molecular mechanism may be inferred from such a fit. This is why we instead propose in the main text to quote the half-life as the ESA signals as a meaningful estimate for the excited state lifetime.

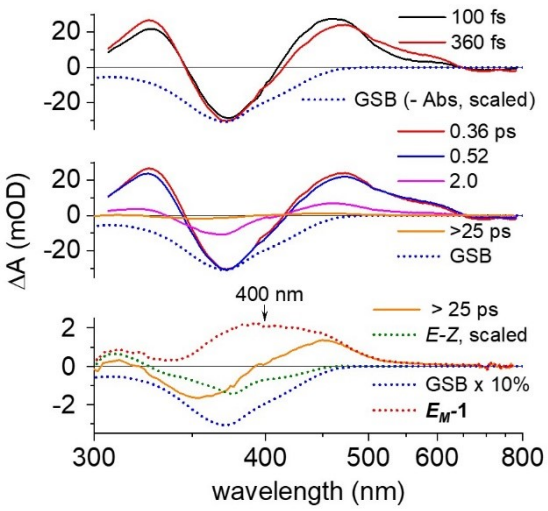

Figure S26. Selection of transient absorption (TA) spectra recorded on ***Z*-1** in methanol upon 400 nm excitation. Top panel: early pump-probe delays (in fs), up to 360 fs. Middle panel: later delays from 360 fs on. In both panels the dashed blue line represents the negative, ground state bleach signal as inferred from the scaled steady state absorption of the ***Z*-1** compound. Bottom panel: quasi-stationary TA spectrum reached after 25 ps (orange) compared with the difference between the E_S**-1** and Z_S**-1** steady-state absorption spectra (green dotted line). The GSB contribution beyond 25 ps is estimated to ~10% of what it is the early TA spectra. The absorption spectrum of the photoproduct - assigned to the metastable *E* isomer E_M**-1**- is computed as the difference between orange and dotted blue lines. It has a maximum at ~400 nm.

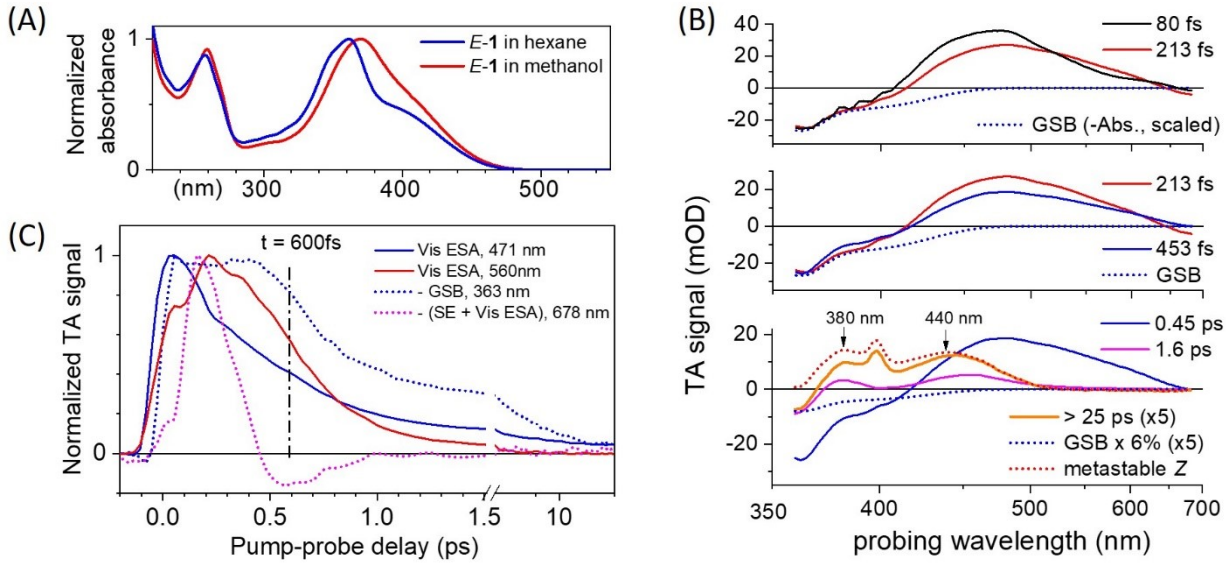

Figure S27. TA spectroscopy of ***E*-1** in hexane upon 400 nm excitation. (A) Steady-state absorption spectrum of ***E*-1** in hexane (blue, λ_{max} = 361 nm), as compared to methanol (red, λ_{max} = 370 nm). (B) Selection of transient absorption TA spectra recorded on ***E*-1** in hexane. Top: At early pump-probe delays, the GSB is observed at λ <410 nm, the Vis ESA (max at ~480nm) redshifts within the first 200 fs and the weak SE signal rises at λ >640 nm on the same time scale. Middle: Between 200 fs and 450 fs, the GSB does not recover while the SE decays or redshifts outside the spectroscopic observation window. Bottom: By 1.6 ps the ESA and GSB have significantly decayed indicating the decay to S_0. A quasi-stationary spectrum is formed by 25 ps (orange line, magnified x5), which we attribute to the metastable *Z* isomer,

characterized - in hexane - by two absorption bands peaking at 380 nm and 440 nm (the narrow bump at 400 nm in the 25-ps spectrum is an experimental artifact due to pump light scattering at this wavelength), and overcoming the residual GSB signal, which impairs evaluating the photoisomerization quantum yield (QY) in this case. Only a lower boundary of QY > 6% may tentatively be inferred. (C) Selection of kinetic traces illustrating (i) the slower rise of the red side of the Vis ESA (at 560 nm, solid red line) indicative of spectral redshift, (ii) the delayed rise and rapid decay of the SE signal (purple dotted line) while the GSB signal (blue dotted line) remains constant, (iii) the oscillatory feature in the 560 nm trace. The half-life of the ESA signal at 560 nm is in the range of 500 fs to 600 fs, very similar to the values in methanol.

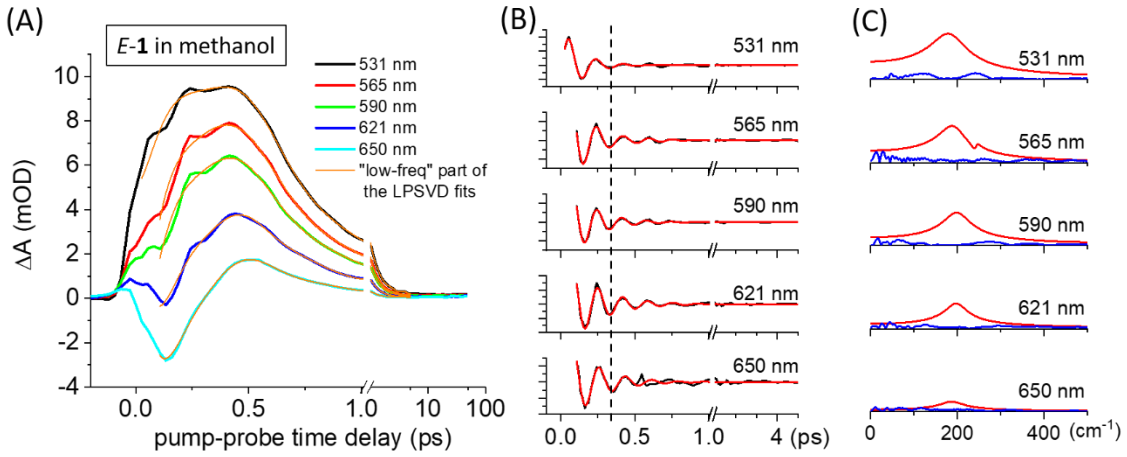

Figure S28. LPSVD analysis of the Vis ESA kinetic traces of ***E*-1** in methanol, evidencing signatures of vibrational coherent motion in S_1. (A) Selection of TA kinetic traces recorded in the low-energy side (>500 nm) of the Vis ESA band. The orange lines are reconstructed including only the frequency components <100 cm^{-1} of the signal, as given by the LPSVD analysis. (B) The oscillatory part of the TA signal (black lines, computed as the difference between the TA kinetics and the orange curves in panel A) are compared with the high-frequency part (>100 cm^{-1} only, red curves) of the LPSVD fit. (C) LPSVD spectrum of the red traces in panel B, compared with the Fourier transform (FFT) of the residuals of the LPSVD fit. The spectral amplitude associated to the dominating oscillatory component is about 3 to 10 times larger than the average amplitude of the fit residuals.

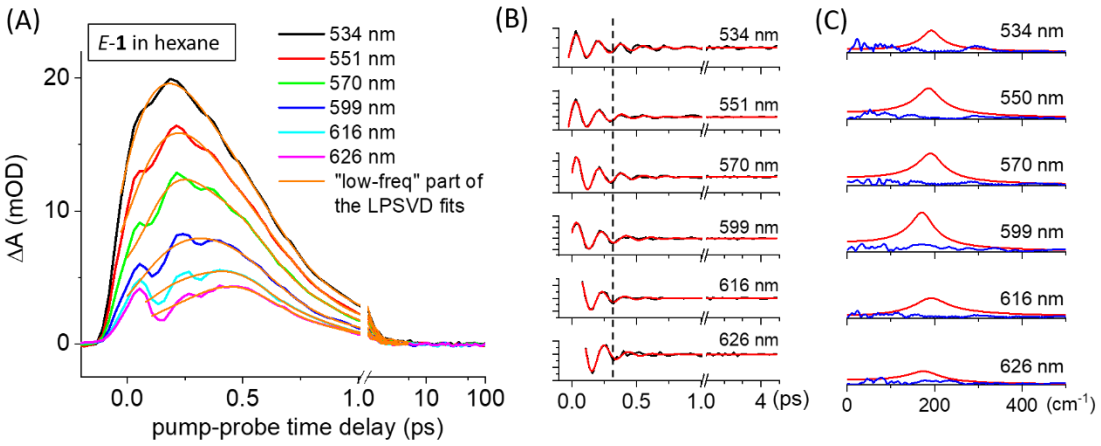

Figure S29. LPSVD analysis of the Vis ESA kinetic traces of ***E*-1** in hexane, evidencing signatures of vibrational coherent motion in S_1. (A) Selection of TA kinetic traces recorded in the low-energy side (>500 nm) of the Vis ESA band. The orange lines are reconstructed including only the frequency components <100 cm^{-1} of the signal, as given by the LPSVD analysis. (B) The oscillatory part of the TA signal (black lines, computed as the difference between the TA kinetics and the orange curves in panel A) are compared with the high-frequency part (>100 cm^{-1} only, red curves) of the LPSVD fit. (C) LPSVD spectrum of the red traces in panel B, compared with the Fourier transform (FFT) of the residuals of the LPSVD fit. The spectral amplitude associated to the dominating oscillatory component is about 3 to 10 times larger than the average amplitude of the fit residuals.

8.3. Analysis of oscillatory signals

Table S2: Frequencies and damping times of the oscillatory signals observed in the Vis ESA band and analysed by LPSVD. Error bars are determined to include all the results obtained from the fit of all decay kinetics shown in Figures 5 (***Z*S-1** in methanol), S26 (***E*S-1** in methanol) and S27 (***E*S-1** in hexane).

	***Z*S-1** in methanol		***E*S-1** in methanol	***E*S-1** in hexane
	Vis ESA <500 nm	Vis ESA >500 nm	Vis ESA >500 nm	Vis ESA >500 nm
Frequency (cm^{-1})	215 ± 8		190 ± 10	185 ± 12
Damping time (fs)	400 ± 40	140 ± 10	170 ± 40	200 ± 60

For ***Z*S-1** in methanol, the oscillations being out-of-phase in the blue and red sides of the ESA band (spectroscopic signature of S_1) is a priori a strong argument in favour of assigning these oscillations to S_1 vibrational activity[14,15]. However, we note that the damping time constant of the oscillatory signal is shorter (140 fs) in the red side of the ESA band, than in its blue side (400 fs). Since the blue side of the Vis ESA band also overlaps with the red side of the GSB, one may not exclude that the longer-lived oscillation observed at λ <500 nm could be an S_0 signature, resulting from Resonant Impulsive Stimulated Raman scattering (RISRS),[16–20] while only the shorter-lived oscillation observed at λ>500nm (i.e. in a spectral region distinct from the GSB) would be an S_1 signature. For ***E*S-1** in methanol and hexane, similar oscillations are detected only in the red side of the ESA band, i.e. in a spectral region distinct from the GSB, and are therefore assigned to S_1 vibrational activity.

9. Computational investigations

All cartesian coordinates are provided as additional supplementary files.

9.1. Photochemical isomerization pathway

The photochemical isomerization pathway of molecule **1** was studied using OpenMolcas (Ver. 19.11).[21,22] The procedure used for the calculations is CASSCF, a multiconfigurational ab initio method (MCSCF) which makes use of all the configurations involving a set of molecular orbitals (MOs, the so-called active space) and a given number of electrons. Hence, this set of configurations is dubbed CASSCF(n,m) where n is the number of electrons and m the number of orbitals involved (both occupied and virtual)[23]. Due to the extended π system in the motor, we found that the minimal active space able to afford an acceptable quality/cost ratio was CASSCF(12,12), as a modification of the active spaces proven to be adequate for similar systems.[24] State average over the lower three singlet roots (SA3) was employed for stationary point and conical intersection optimizations. For the latter, the analytical nonadiabatic coupling vectors search implemented in OpenMolcas was used.[25] Numerical frequencies were employed to characterize the stationary points.

The conical intersections and the minima were then connected with a linear interpolation of internal coordinates as implemented in ASE.[26] Optimizations at the S_0 and S_1 were run on these guess structures, the torsion dihedral angle to limit the occurrence of discontinuities in the energy surfaces, due to the mobility of the upper-half five-membered ring ($C_AC_BC_CC_D$, Scheme S1).

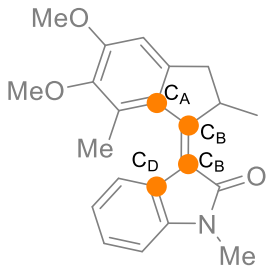

Scheme S1.

The extended multistate second-order perturbation XMS-CASPT2[27–29] on the lowest four singlet states was employed to retrieve the dynamic correlation. To avoid the presence of intruder states, an imaginary shift to the external part of the zeroth order Hamiltonian of 0.1 Hartree was introduced, while no IPEA shift was added. Oscillator strengths for the vertical transitions were calculated at this level of theory via the RASSI module in OpenMolcas.

The charges in Figure 7 of the main text were calculated at the SF-BH&HLYP/cc-pVDZ level over three roots, as implemented in GAMESS-US (Ver: 30 SEP 2020 (R2)).[30]

The deformations associated to the branching plane are also provided as animated gif image as additional Supporting file.

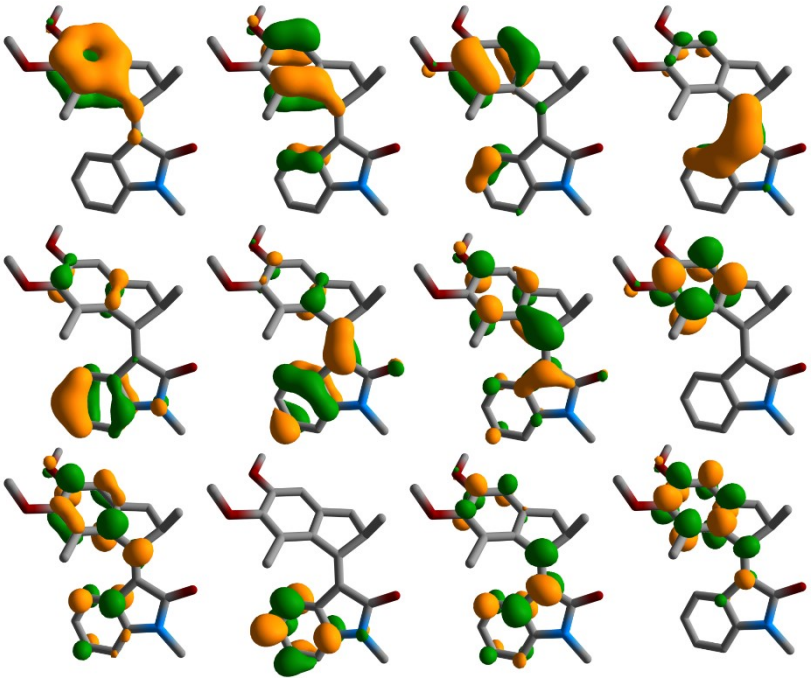

Figure S30. Active space used in the XMS-CASPT2/CASSCF calculations.

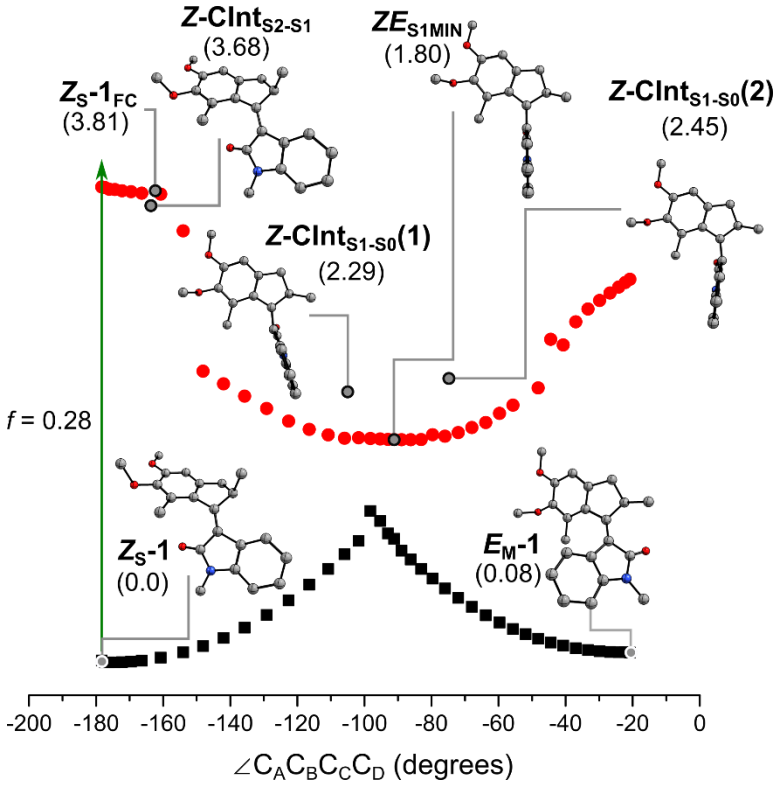

Figure S31. Photochemical Z-E isomerization of compound 1 at the XMS-CASPT2/6-31G*//CASSCF(12,12)/6-31G* level. The figure represents the relaxed scans of the stable Z to unstable E photochemical reaction on different excited state surfaces. The energies were calculated as a single point XMS-CASPT2/6-31G* energy calculation over the four lower singlets on the geometries optimised at the SA3-CASSCF(12,12)/6-31G* level, either at the ground state (back squares) or the first excited state (red dots).

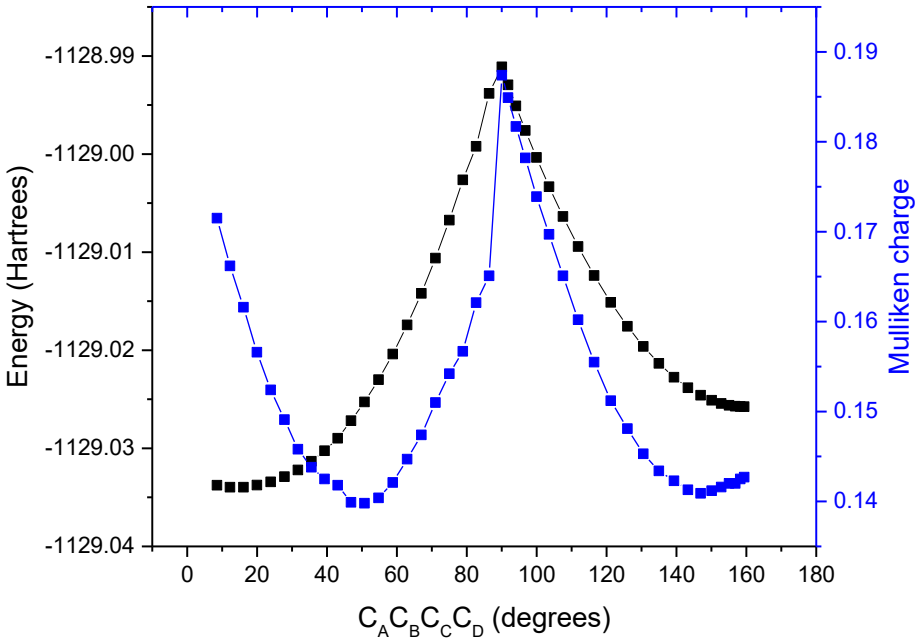

Figure S32. Mulliken charges (in blue) on the lower half of motor **1** at the S_0 following the E-Z isomerization, plotted together with the energy of the system (black), at the XMS-CASPT2/6-31G//CASSCF(12,12)/6-31G* level.

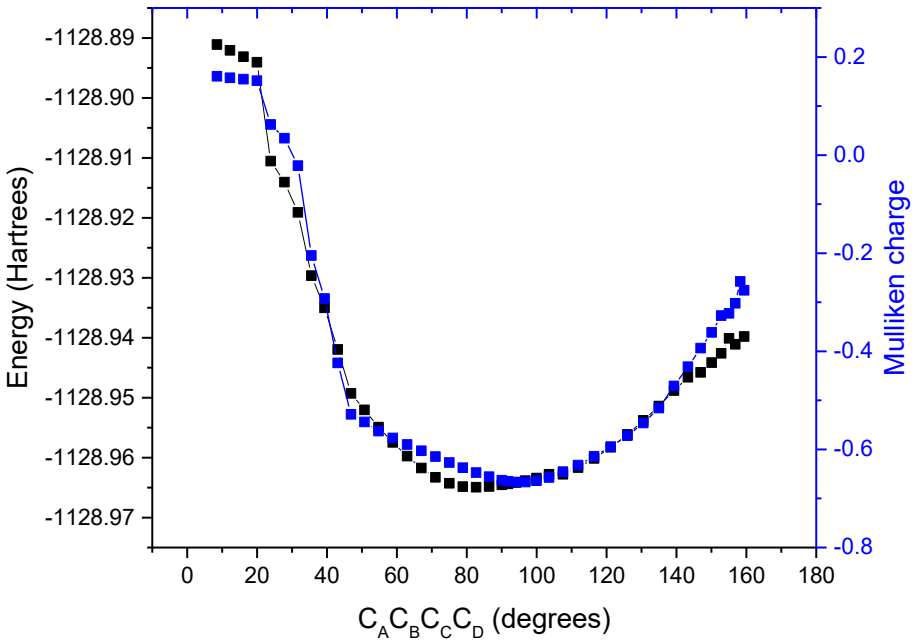

Figure S33. Mulliken charges (in blue) on the lower half of motor **1** at the S_1 following the E-Z isomerization, plotted together with the energy of the system (black), at the XMS-CASPT2/6-31G//CASSCF(12,12)/6-31G* level.

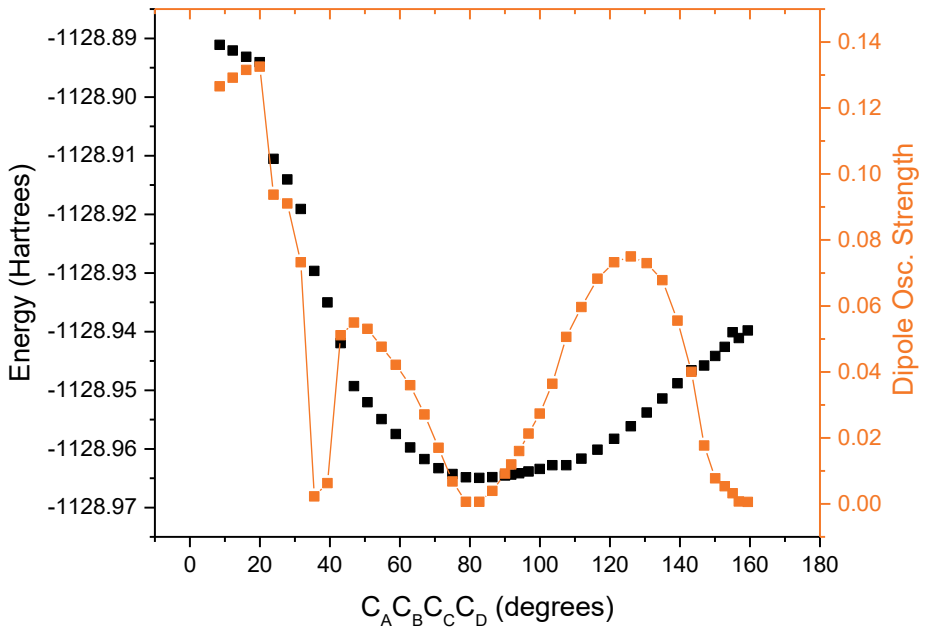

Figure S34. Dipole oscillator strength (in orange) for the $S_1 \rightarrow S_0$ transition following the E-Z isomerization, plotted together with the energy of the system (black), at the XMS-CASPT2/6-31G//CASSCF(12,12)/6-31G* level.

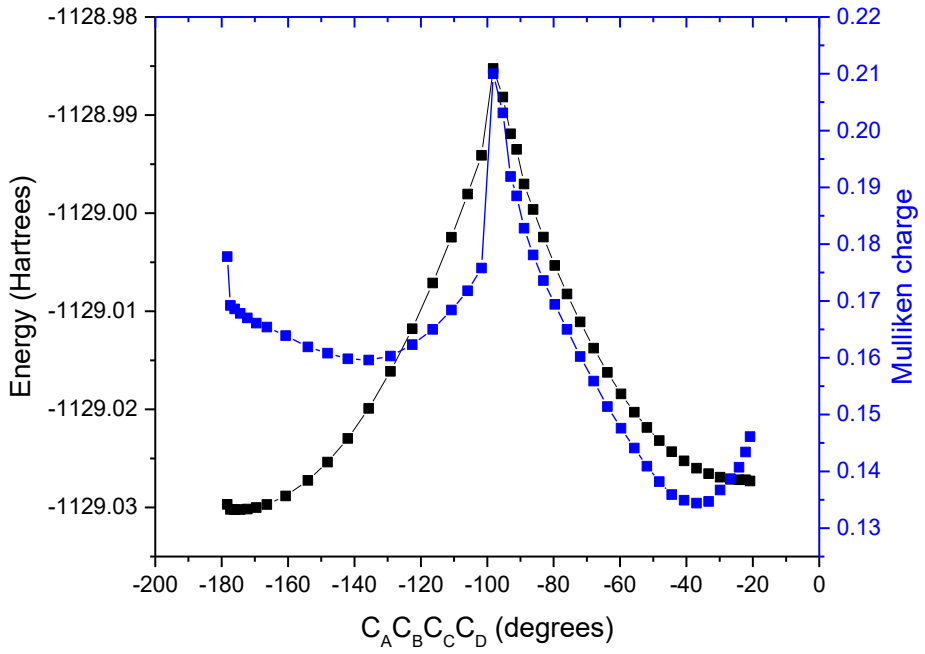

Figure S35. Mulliken charges (in blue) on the lower half of motor **1** at the S_0 following the Z-E isomerization, plotted together with the energy of the system (black), at the XMS-CASPT2/6-31G//CASSCF(12,12)/6-31G* level.

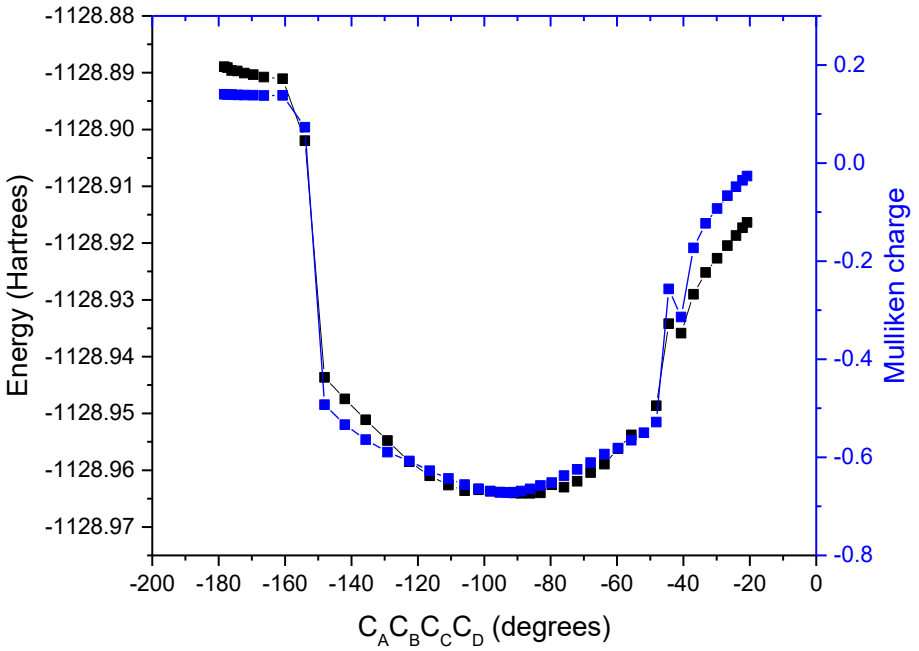

Figure S36. Mulliken charges (in blue) on the lower half of motor **1** at the S_1 following the Z-E isomerization, plotted together with the energy of the system (black), at the XMS-CASPT2/6-31G//CASSCF(12,12)/6-31G* level.

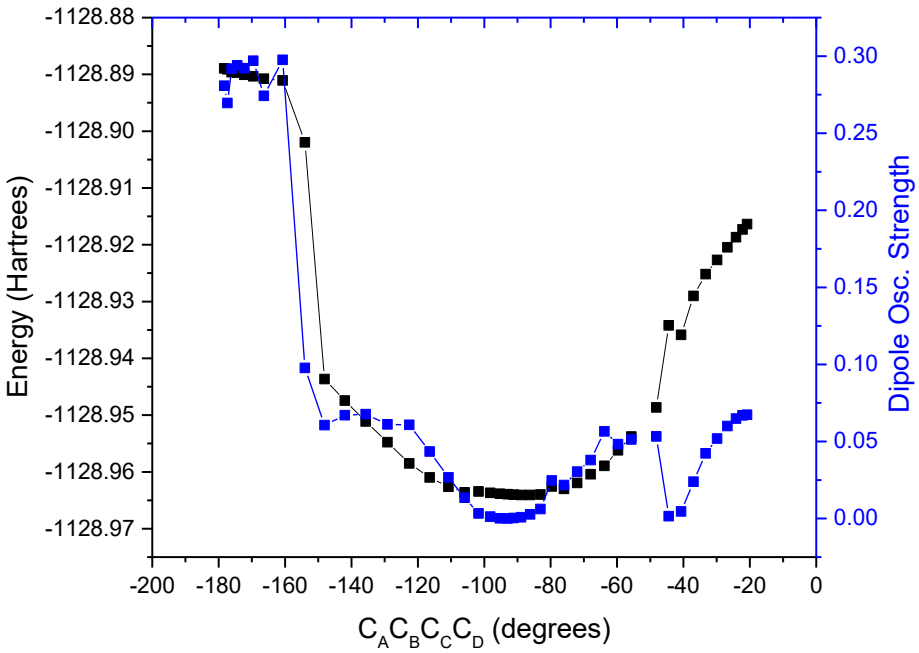

Figure S37. Dipole oscillator strength (in blue) for the $S_1 \rightarrow S_0$ transition following the Z-E isomerization, plotted together with the energy of the system (black), at the XMS-CASPT2/6-31G//CASSCF(12,12)/6-31G* level.

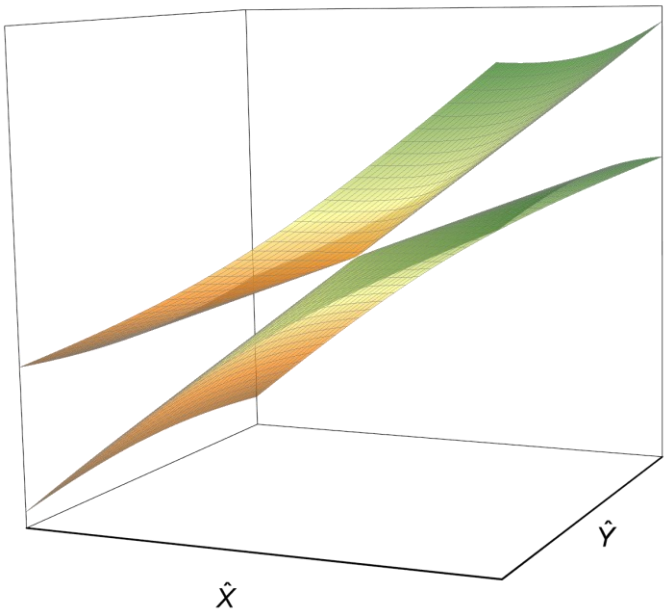

Figure S38. Branching plane of **CInt$_{S1\text{-}S0}$(2)**. The conical intersection has a sloped topology.

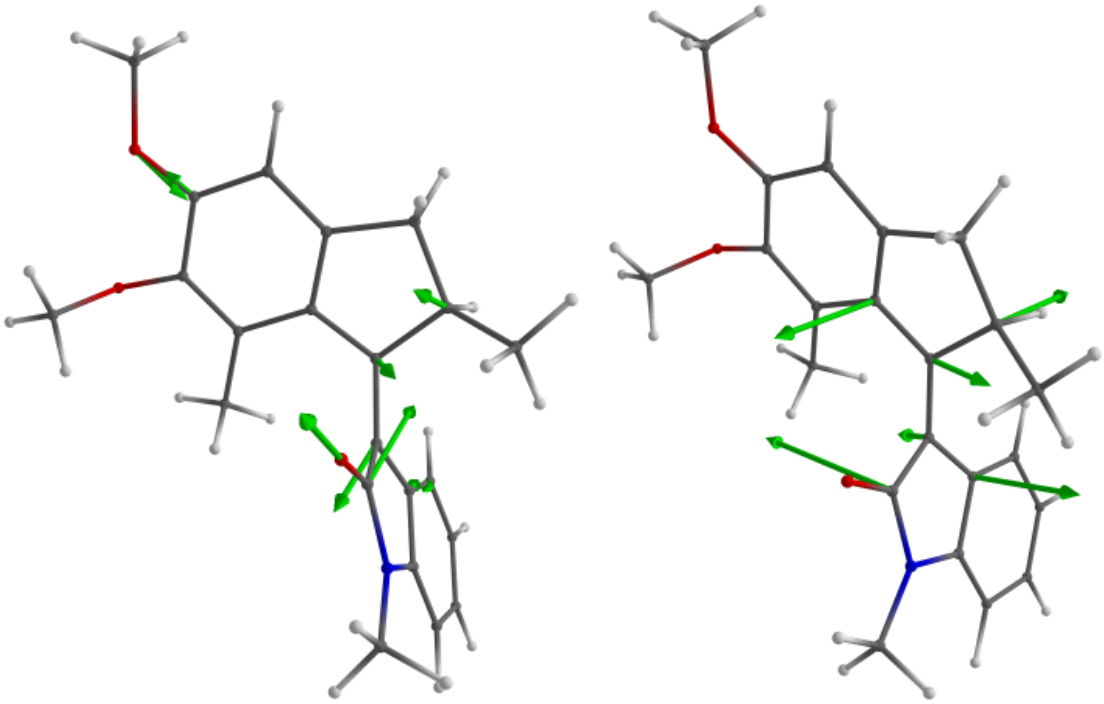

Figure S39. $\hat{x}$ (left) and $\hat{y}$ (right) branching plane vectors of **CInt$_{S1\text{-}S0}$(2)**. Vector $\hat{x}$ features the pyramidalisation distortion typical of the alkene branching plane, while vector $\hat{y}$ describes the C_B=C_C bond twisting associated with the rotation.

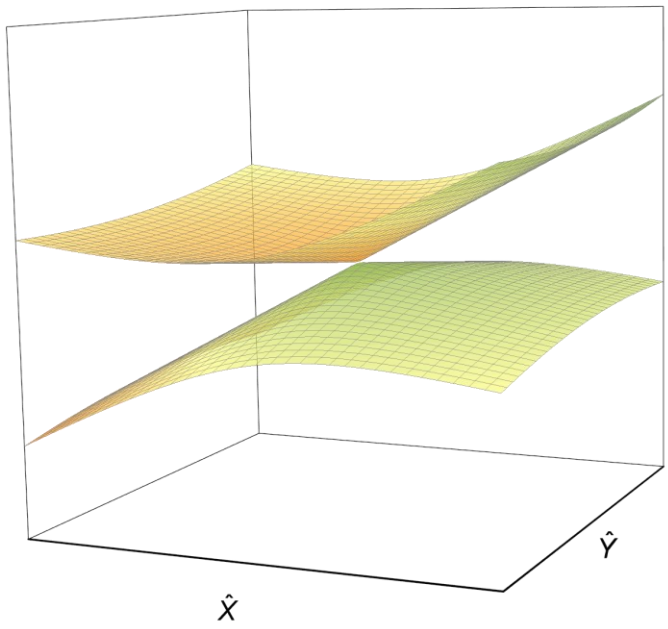

Figure S40. Branching plane of **CInt**$_{S2\text{-}S1}$. The conical intersection has a peaked topology.

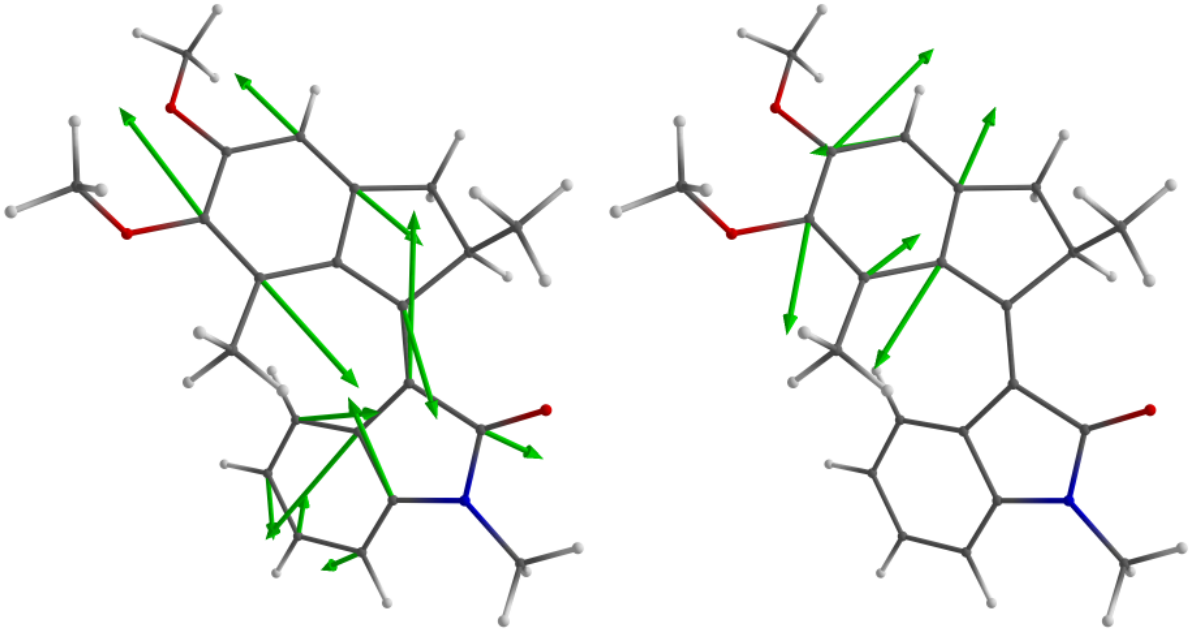

Figure S41. $\hat{x}$ (left) and $\hat{y}$ (right) branching plane vectors of **CInt**$_{S2\text{-}S1}$. Both vector $\hat{x}$ and vector $\hat{y}$ describe bond length alternations: the former along the entire π scaffold, the latter only on the rotor aryl ring.

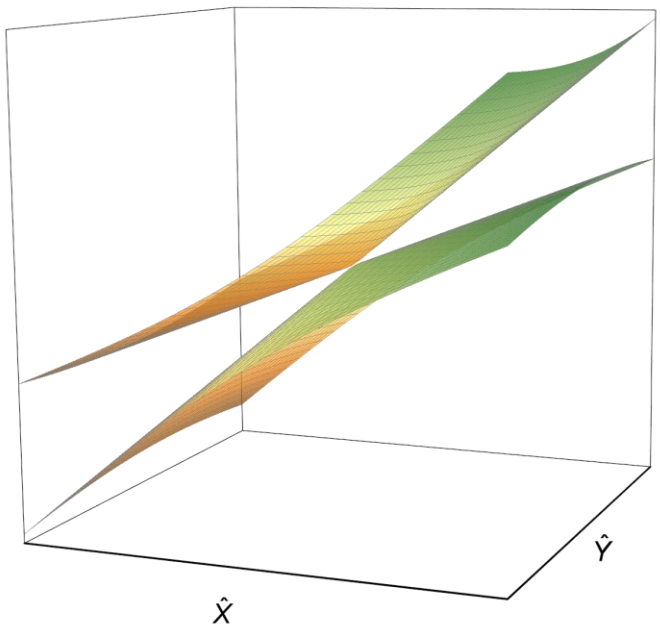

Figure S42. Branching plane of ***Z*-CInt$_{S1\text{-}S0}$(1)**. The conical intersection has a sloped topology.

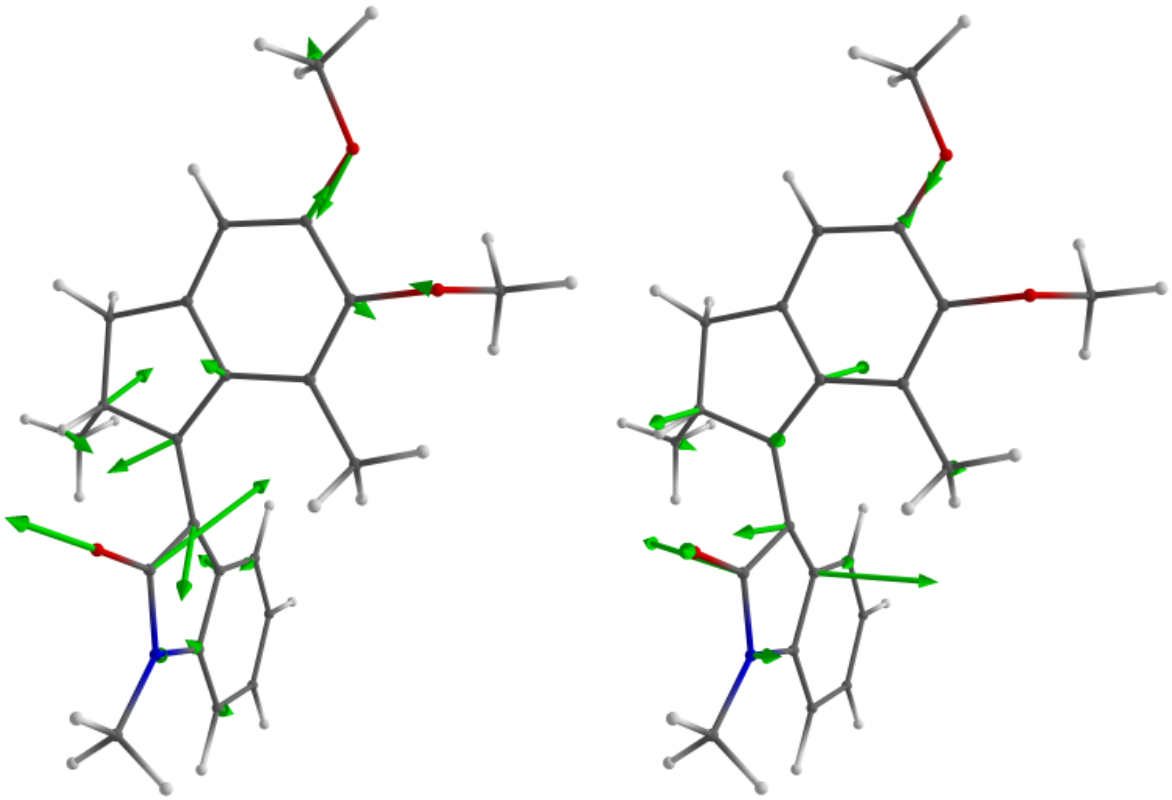

Figure S43. $\hat{x}$ (left) and $\hat{y}$ (right) branching plane vectors of ***Z*-CInt$_{S1\text{-}S0}$(1)**. Vector $\hat{x}$ features the pyramidalisation distortion typical of the alkene branching plane, while vector $\hat{y}$ describes the C_B=C_C bond twisting associated with the rotation.

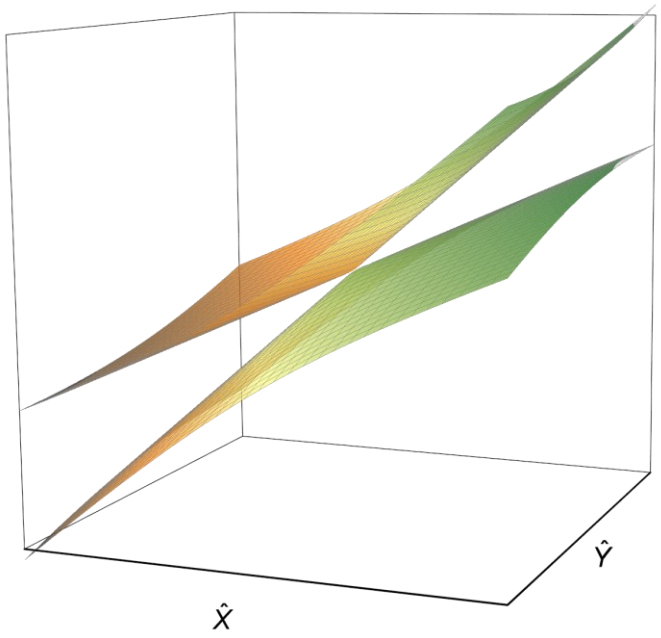

Figure S44. Branching plane of ***Z*-CInt$_{S1\text{-}S0}$(2)**. The conical intersection has a sloped topology.

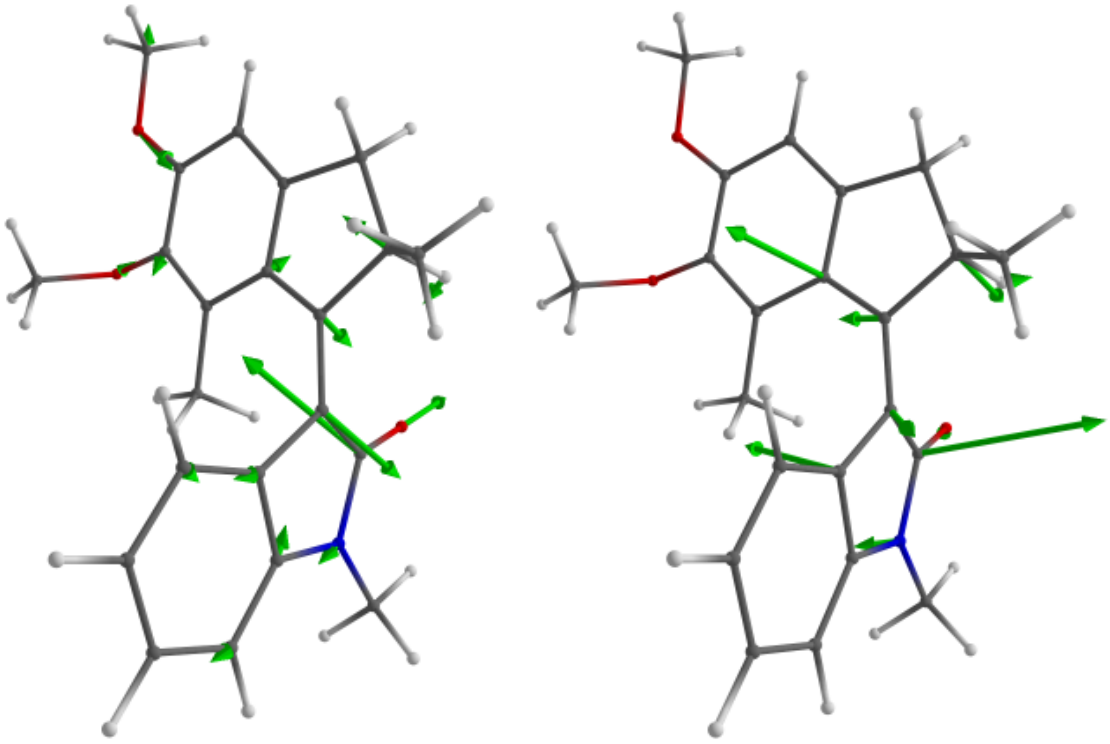

Figure S45. $\hat{x}$ (left) and $\hat{y}$ (right) branching plane vectors of ***Z*-CInt$_{S1\text{-}S0}$(2)**. Vector $\hat{x}$ features the pyramidalisation distortion typical of the alkene branching plane, while vector $\hat{y}$ describes the C_B=C_C bond twisting associated with the rotation.

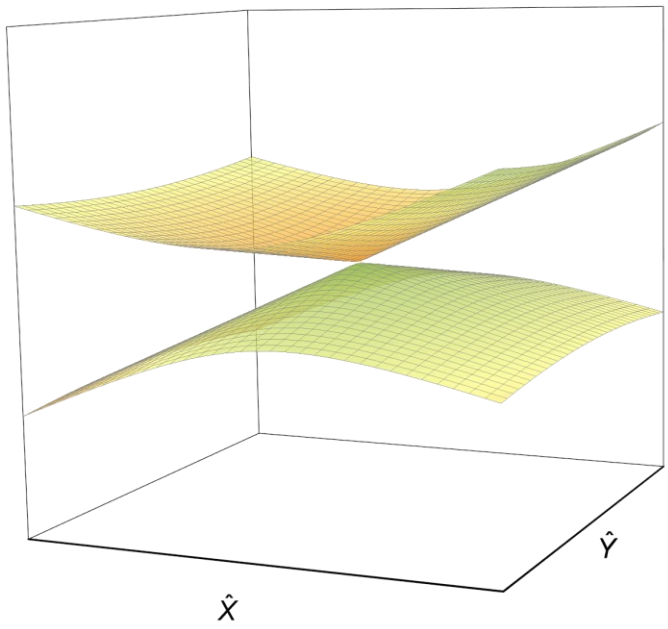

Figure S46. Branching plane of ***Z*-CInt$_{S2\text{-}S1}$**. The conical intersection has a peaked topology.

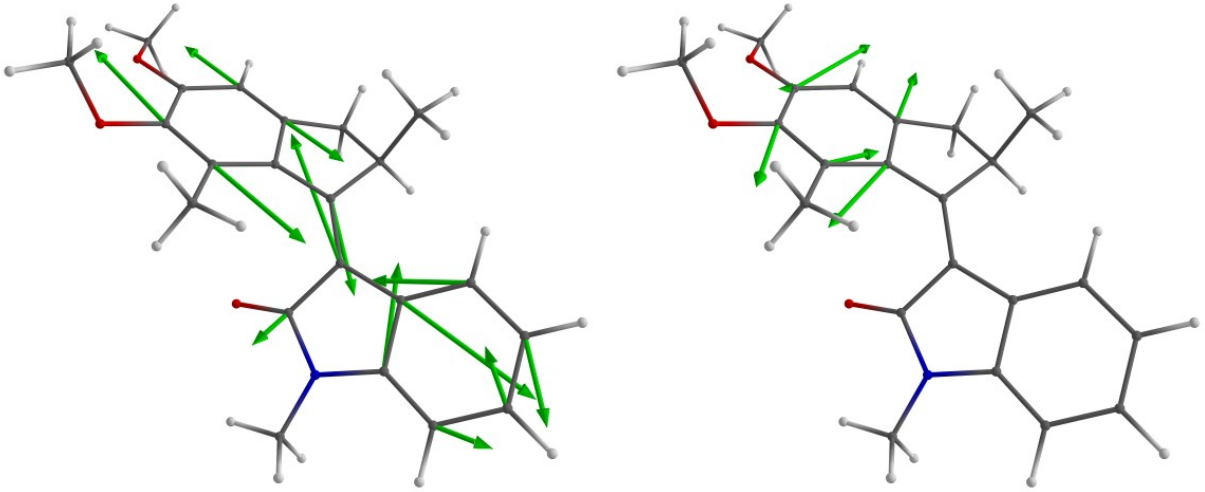

Figure S47. $\hat{x}$ (left) and $\hat{y}$ (right) branching plane vectors of ***Z*-CInt$_{S2\text{-}S1}$**. Both vector $\hat{x}$ and vector $\hat{y}$ describe bond length alternations: the former along the entire π scaffold, the latter only on the rotor aryl ring.

9.2. Frequency calculations

The normal modes of vibration for the local (Franck Condon) minima of the S1 state of *E*-*Z* and *Z*-*E* paths were calculated numerically at the CASSCF(12,12)/6-31G* level (for ***E*S-1FC**) and analytically at the TD(5states)-ωB97X-D/def2-SVP level (for ***E*S-1FC** and ***Z*S-1FC**), on the optimized geometries obtained with the respective methods. Both methods furnish very similar geometries for the minima considered, confirming the validity of the ωB97X-D functional to describe the excited state of photoactuators.[31] All the DFT and TD-DFT calculations were performed using Gaussian Ver. B.01.[32]

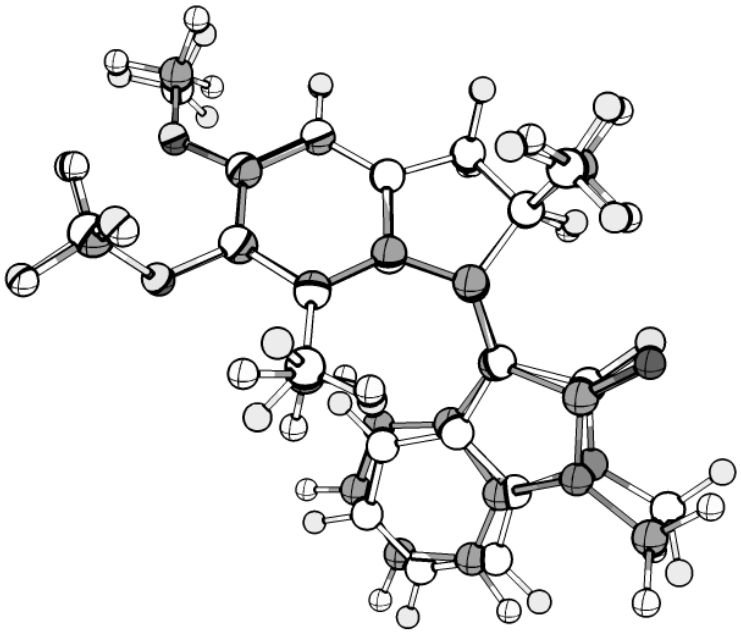

Figure S48. Comparison of ***E*S-1FC** obtained at the CASSCF(12,12)/6-31G* and TD-ωB97X-D/def2-SVP level of theory. The superposition of the geometry at the CASSCF level (in white) and TD-DFT level (in grey) gives an RMSD = 0.364.

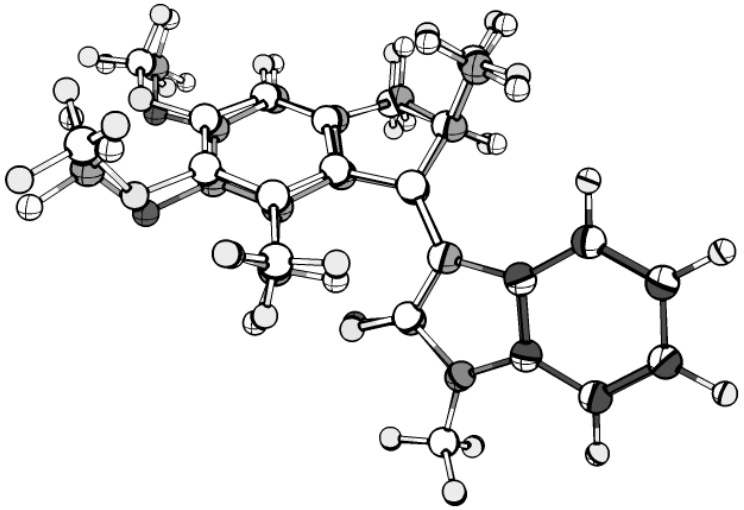

Figure S49. Comparison of ***Z*S-1FC** obtained at the CASSCF(12,12)/6-31G* and TD-ωB97X-D/def2-SVP level of theory. The superposition of the geometry at the CASSCF level (in white) and TD-DFT level (in grey) gives an RMSD = 0.169.

We identified a normal mode of vibration of ***E*S-1FC** – mode ν_{16} - at 200 cm^{-1} at the TD-ωB97X-D/def2-SVP level, (see Figure 7; the same mode is also calculated at 200 cm^{-1} at the CASSCF level) showing a rocking motion of the Cα carbon of the stator towards a more planar ring structure with the associated diminished pyramidalization of C_C. The movement is accompanied by a synchronous motion of the methyl on C_E.

After visual inspection of ν_{16}, we suggest that this mode mostly corresponds to the deformation connecting the Franck Condon point (corresponding to the ground state minimum) to the ***E*S-1FC** region. Interestingly, the ν_{16} modes is also predicted at the geometry of ***EZ*-S1MIN** and associated with a value of 206 cm^{-1}). These modes can be better appreciated in a gif animated image provided as additional file (E-nu16.gjf and Z-nu16.gjf, along with the deformation from the FC point to the FC minimum: E-FC-to-FCmin.gif and Z-FC-to-FCmin.gif).

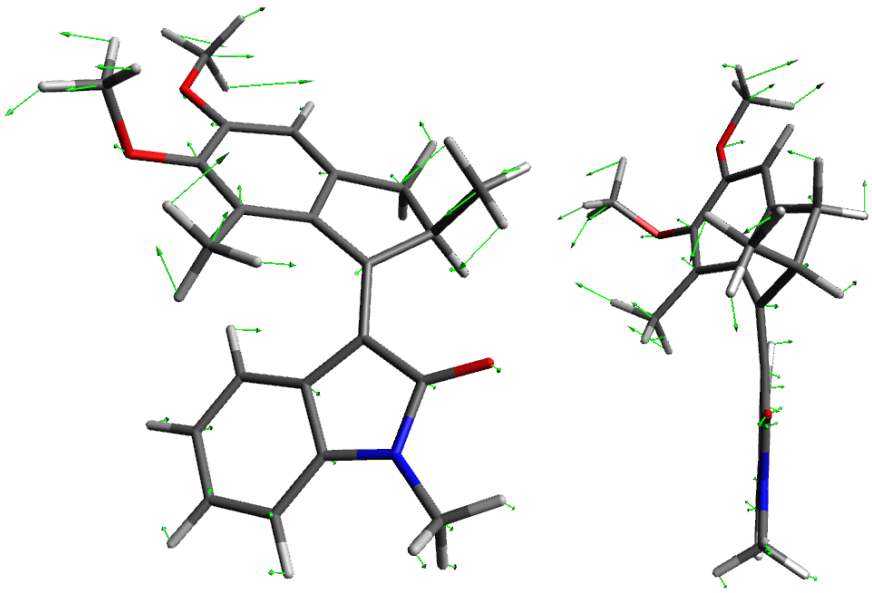

Figure S50. Force vectors for the 199.84 cm^{-1} mode (ν_{16}) of $\boldsymbol{E}_{S}$**-1**$_{FC}$ at the TD-ωB97X-D/def2-SVP. The mode is affected strongly by the vibration of the five-membered ring and pyramidalization of the alkene carbons.

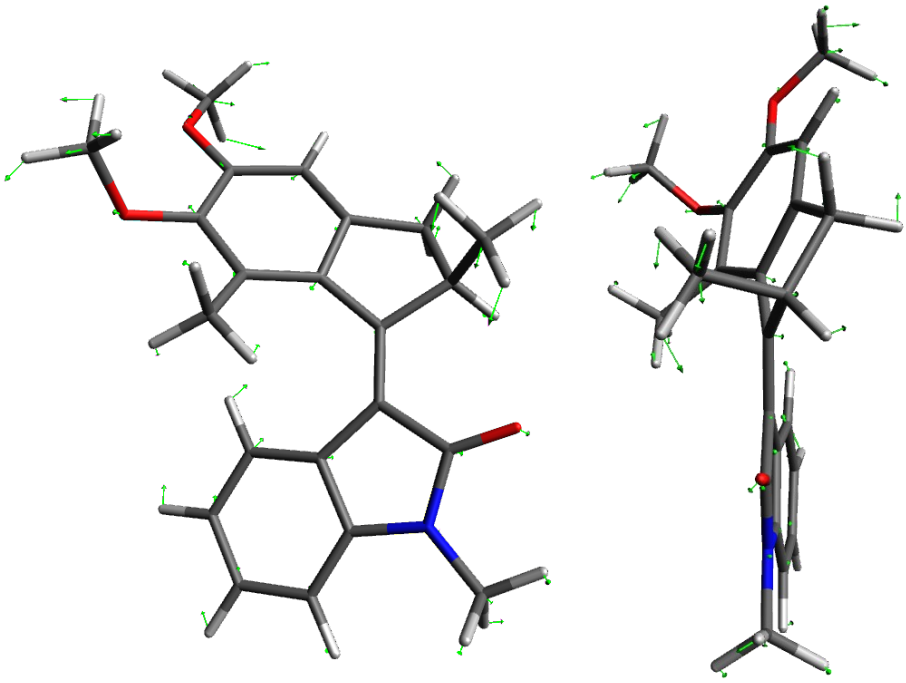

Figure S51. Force vectors for the 199.86 cm^{-1} mode (ν_{16}) of $\boldsymbol{E}_{S}$**-1**$_{FC}$ at the CASSCF(12,12)/6-31G*. The mode is affected strongly by the vibration of the five-membered ring and pyramidalization of the alkene carbons.

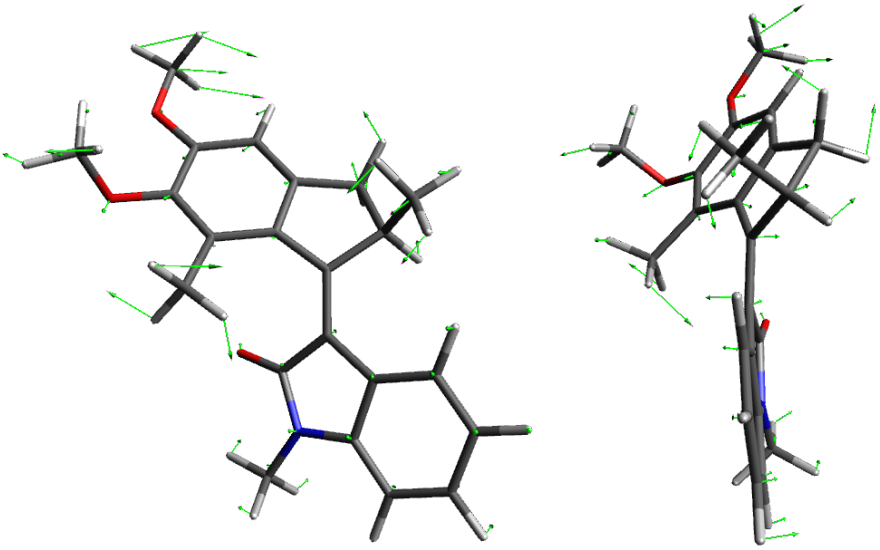

Figure S52. Force vectors for the 209.96 cm^{-1} mode (ν_{16}) of $\boldsymbol{Z}_{\mathbf{S}}$**-1**$_{\mathbf{FC}}$ at the TD-ωB97X-D/def2-SVP. The mode is affected strongly by the vibration of the five-membered ring and pyramidalization of the alkene carbons.

9.3. Thermal isomerization, CD and UV-Vis spectra simulation.

The thermal helix inversion steps were evaluated using MP2/6-31G* and compared to the results obtained from the DFT at the ωB97X-D/6-31G*, ωB97X-D/def2-SVP and ωB97X-D/def2-TZVP as implemented in Gaussian 16, Rev. B01.[32] The solvent effect of methanol was introduced using the implicit PCM method for both optimizations and further spectroscopic simulations. The UV-Vis and CD (for the latter see section 4 of this SI) spectra of the stable and unstable species were computed as a single point calculation on the MP2/6-31G* geometries at the TD-ωB97X-D/6-311+G(2d,p) level, over the lower 25 transitions. In all cases, $\Delta G^{\ddagger}$ for TSZ is ca. 14-15 kcal · mol^{-1}, ca. 1 kcal · mol^{-1} lower than $\Delta G^{\ddagger}$ for TSE. These results match the trend observed with the low temperature NMR measurements.

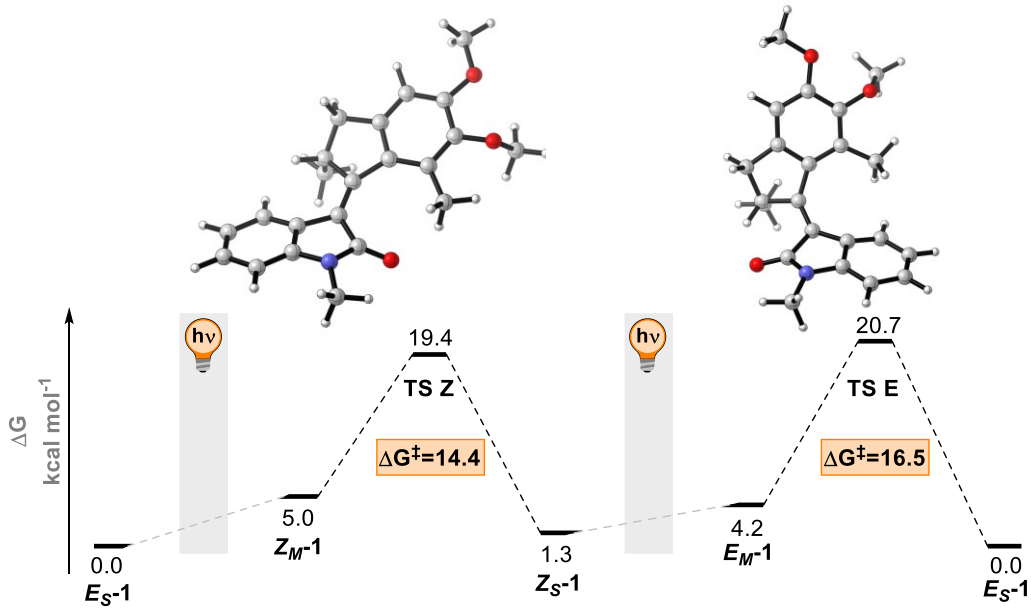

Figure S53. Thermal barriers for the THI processes at the PCM(MeOH)-MP2/6-31G* level. The geometries of the transition state for the unstable Z to stable Z (TSZ) transformation and the one for the unstable E to stable Z (TSE) one are depicted.

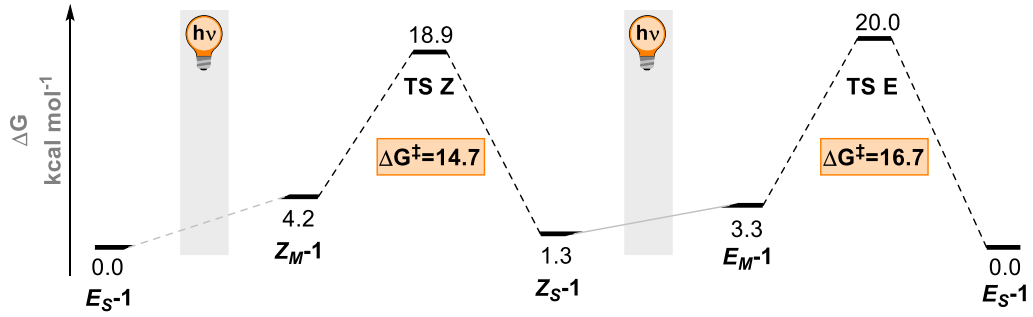

Figure S54. Thermal barriers for the THI processes at the PCM(MeOH)-ωB97X-D/6-31G* level.

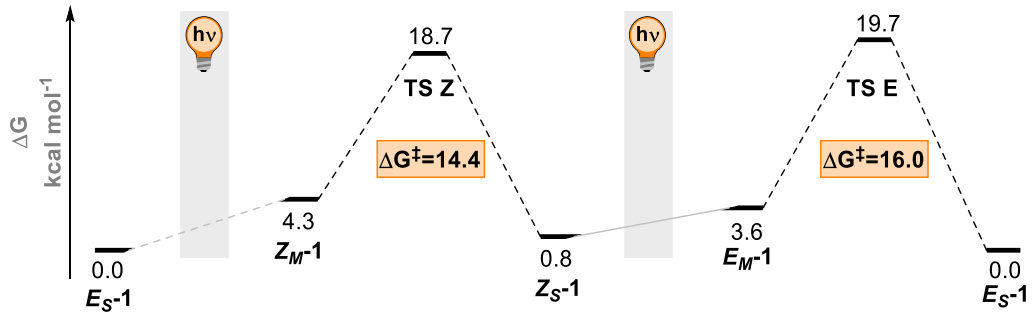

Figure S55. Thermal barriers for the THI processes at the PCM(MeOH)-ωB97X-D/def2-SVP level.

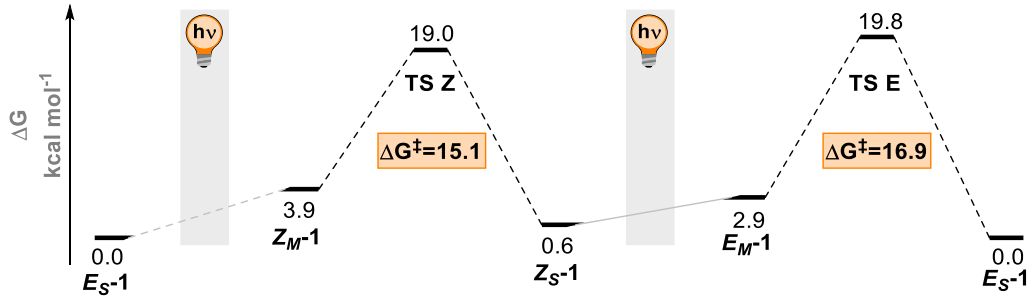

Figure S56. Thermal barriers for the THI processes at the PCM(MeOH)-ωB97X-D/def2-TZVP level.

Table S3. Experimental and calculated Gibbs free energy barriers (kcal·mol^{-1}) of thermal helix inversion and half-lives of the respective metastable states of motor **1**. For all these calculations the PCM (MeOH) implicit solvation model was used.

	$\Delta G^{\ddagger}$ ***Z*M-1→*Z*S-1**	$\Delta G^{\ddagger}$ ***E*M-1→*E*S-1**
Exp.	11.8	17.4
MP2/6-31G(d)	14.4	16.5
ωB97X-D/6-31G(d)	14.7	16.7
ωB97X-D/def2-SVP	14.4	16.2
ωB97X-D/def2-TZVP	15.1	16.9

UV-Vis spectra at the PCM(MeOH)-TD-ωB97X-D/6-311+G(2d,p)// PCM(MeOH)-MP2/6-31G* level.

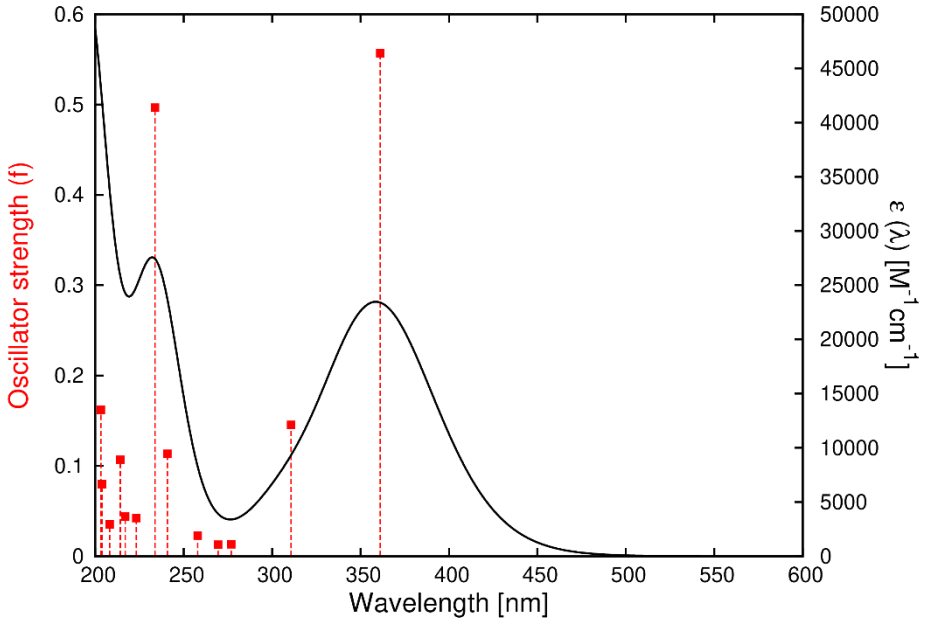

Figure S57. Simulated UV-Vis spectrum of stable ***E*s-1**. The values associated to the lowest five transitions are reported below.

Excited State 1: 3.4333 eV 361.12nm f=0.5569
Excited State 2: 3.9896 eV 310.77nm f=0.1455
Excited State 3: 4.4773 eV 276.92nm f=0.0131
Excited State 4: 4.6000 eV 269.53nm f=0.0129
Excited State 5: 4.8067 eV 257.94nm f=0.0227

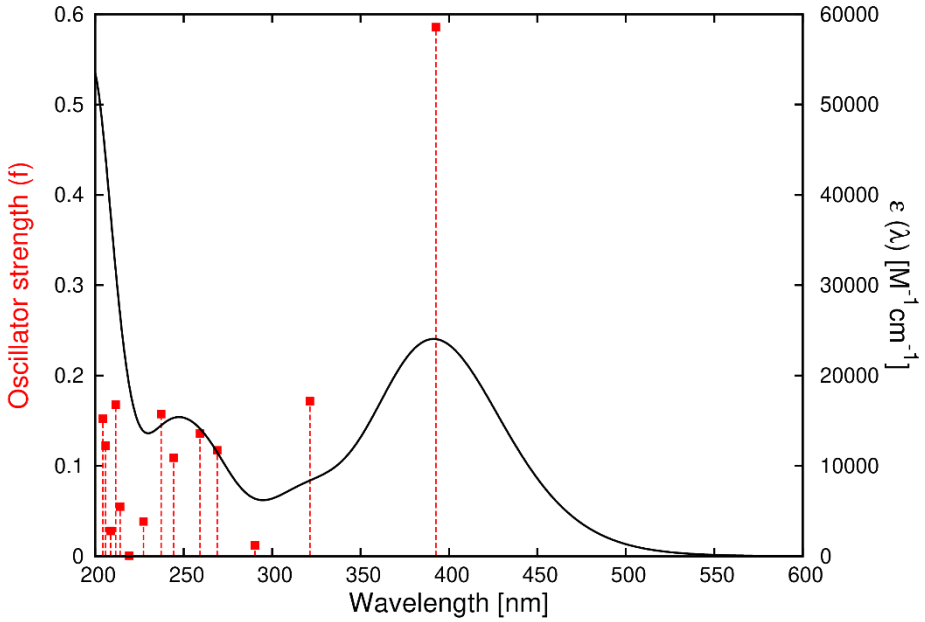

Figure S58. Simulated UV-Vis spectrum of metastable Z_M-**1**. The values associated to the lowest five transitions are reported below.

Excited State 1: 3.1581 eV 392.60nm f=0.5856
Excited State 2: 3.8582 eV 321.36nm f=0.1714
Excited State 3: 4.2714 eV 290.27nm f=0.0119
Excited State 4: 4.6093 eV 268.99nm f=0.1172
Excited State 5: 4.7830 eV 259.22nm f=0.1358

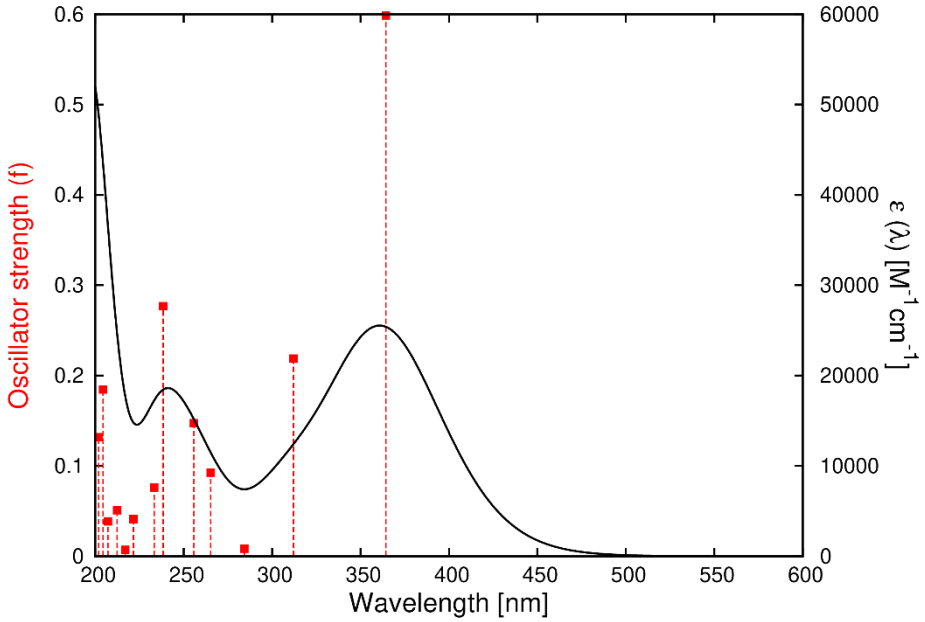

Figure S59. Simulated UV-Vis spectrum of stable ***Z*S-1**. The values associated to the lowest five transitions are reported below.

Excited State 1: 3.4035 eV 364.28nm f=0.5985
Excited State 2: 3.9732 eV 312.05nm f=0.2188
Excited State 3: 4.3606 eV 284.33nm f=0.0083
Excited State 4: 4.6737 eV 265.28nm f=0.0925
Excited State 5: 4.8477 eV 255.76nm f=0.1472

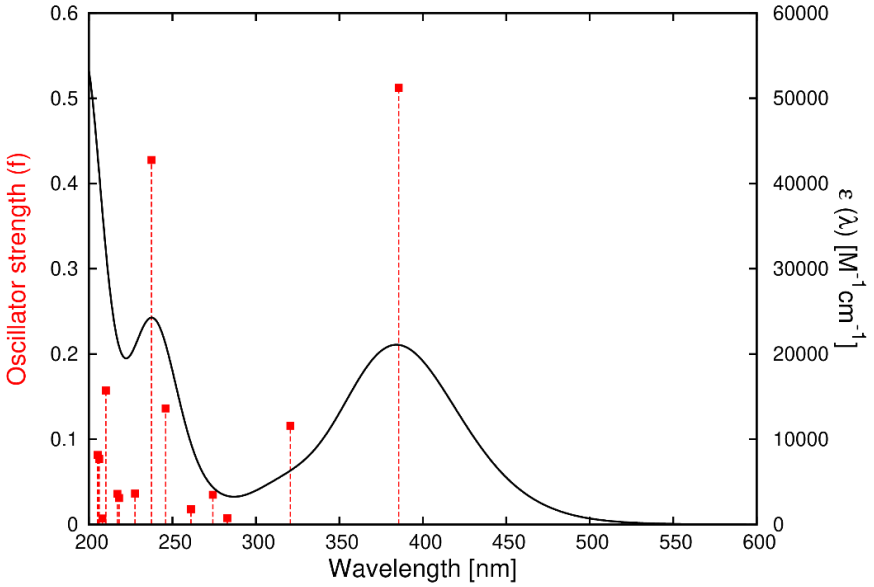

Figure S60. Simulated UV-Vis spectrum of metastable ***E*M-1**. The values associated to the lowest five transitions are reported below.

Excited State 1: 3.2157 eV 385.56nm f=0.5120
Excited State 2: 3.8657 eV 320.73nm f=0.1158
Excited State 3: 4.3848 eV 282.76nm f=0.0075
Excited State 4: 4.5208 eV 274.25nm f=0.0348
Excited State 5: 4.7480 eV 261.13nm f=0.0179

References

1 G. London, G. T. Carroll, T. Fernández Landaluce, M. M. Pollard, P. Rudolf and B. L. Feringa, *Chem. Commun.*, 2009, 1712–1714.

2 Bruker, APEX3 (V2019.1-0), SAINT (Version 8.40A) and SADABS (Version 2016/1). Bruker AXS Inc., Madison, Wisconsin, USA.

3 L. Krause, R. Herbst-Irmer, G. M. Sheldrick and D. Stalke, *J. Appl. Crystallogr.*, 2015, **48**, 3–10.

4 G. M. Sheldrick and IUCr, *Acta Crystallogr. Sect. A Found. Adv.*, 2015, **71**, 3–8.

5 G. M. Sheldrick, *Acta Crystallogr Sect. A*, 2008, **A64**, 112–122.

6 A. L. Spek, *J. Appl. Crystallogr.*, 2003, **36**, 7–13.

7 L. N. Lameijer, S. Budzak, N. A. Simeth, M. J. Hansen, B. L. Feringa, D. Jacquemin and W. Szymanski, *Angew. Chemie Int. Ed.*, 2020, **59**, 21663–21670.

8 K. Stranius and K. Börjesson, *Sci. Rep.*, 2017, **7**, 1–9.

9 H. J. Kuhn, S. E. Braslavsky and R. Schmidt, *Pure Appl. Chem.*, 2004, **76**, 2105–2146.

10 M. Montalti, A. Credi, L. Prodi and M. T. Gandolfi, *Handbook of Photochemistry*, CRC Press, Cleveland OH, 2006.

11 J. Otsuki, K. Suwa, K. K. Sarker and C. Sinha, *J. Phys. Chem. A*, 2007, **111**, 1403–1409.

12 J. Briand, O. Bräm, J. Réhault, J. Léonard, A. Cannizzo, M. Chergui, V. Zanirato, M. Olivucci, J. Helbing and S. Haacke, *Phys. Chem. Chem. Phys.*, 2010, **12**, 3178–3187.

13 A. I. Skilitsi, D. Agathangelou, I. Shulov, J. Conyard, S. Haacke, Y. Mély, A. Klymchenko and J. Léonard, *Phys. Chem. Chem. Phys.*, 2018, **20**, 7885–7895.

14 Q. Wang, R. Schoenlein, L. Peteanu, R. Mathies and C. Shank, *Science*, 1994, **266**, 422–424.

15 M. H. Vos, F. Rappaport, J.-C. Lambry, J. Breton and J.-L. Martin, *Nature*, 1993, **363**, 320–325.

16 J. Chesnoy and A. Mokhtari, *Phys. Rev. A*, 1988, **38**, 3566–3576.

17 L. Dhar, J. A. Rogers and K. A. Nelson, *Chem. Rev.*, 1994, **94**, 157–193.

18 H. L. Fragnito, J.-Y. Bigot, P. C. Becker and C. V. Shank, *Chem. Phys. Lett.*, 1989, **160**, 101–104.

19 W. T. Pollard, H. L. Fragnito, J.-Y. Bigot, C. V. Shank and R. A. Mathies, *Chem. Phys. Lett.*, 1990, **168**, 239–245.

20 S. Ruhman, A. G. Joly and K. A. Nelson, *IEEE J. Quantum Electron.*, 1988, **24**, 460–469.

21 I. Fdez. Galván, M. Vacher, A. Alavi, C. Angeli, F. Aquilante, J. Autschbach, J. J. Bao, S. I. Bokarev, N. A. Bogdanov, R. K. Carlson, L. F. Chibotaru, J. Creutzberg, N. Dattani, M. G. Delcey, S. S. Dong, A. Dreuw, L. Freitag, L. M. Frutos, L. Gagliardi, F. Gendron, A. Giussani,

L. González, G. Grell, M. Guo, C. E. Hoyer, M. Johansson, S. Keller, S. Knecht, G. Kovačević, E. Källman, G. Li Manni, M. Lundberg, Y. Ma, S. Mai, J. P. Malhado, P. Å. Malmqvist, P. Marquetand, S. A. Mewes, J. Norell, M. Olivucci, M. Oppel, Q. M. Phung, K. Pierloot, F. Plasser, M. Reiher, A. M. Sand, I. Schapiro, P. Sharma, C. J. Stein, L. K. Sørensen, D. G. Truhlar, M. Ugandi, L. Ungur, A. Valentini, S. Vancoillie, V. Veryazov, O. Weser, T. A. Wesołowski, P.-O. Widmark, S. Wouters, A. Zech, J. P. Zobel and R. Lindh, *J. Chem. Theory Comput.*, 2019, **15**, 5925–5964.

22 F. Aquilante, J. Autschbach, A. Baiardi, S. Battaglia, V. A. Borin, L. F. Chibotaru, I. Conti, L. De Vico, M. Delcey, I. Fdez. Galván, N. Ferré, L. Freitag, M. Garavelli, X. Gong, S. Knecht, E. D. Larsson, R. Lindh, M. Lundberg, P. Å. Malmqvist, A. Nenov, J. Norell, M. Odelius, M. Olivucci, T. B. Pedersen, L. Pedraza-González, Q. M. Phung, K. Pierloot, M. Reiher, I. Schapiro, J. Segarra-Martí, F. Segatta, L. Seijo, S. Sen, D.-C. Sergentu, C. J. Stein, L. Ungur, M. Vacher, A. Valentini and V. Veryazov, *J. Chem. Phys.*, 2020, **152**, 214117.

23 B. O. Roos, P. R. Taylor and P. E. M. Sigbahn, *Chem. Phys.*, 1980, **48**, 157–173.

24 M. Gueye, M. Manathunga, D. Agathangelou, Y. Orozco, M. Paolino, S. Fusi, S. Haacke, M. Olivucci and J. Leónard, *Nat. Commun.*, 2018, **9**, 1–8.

25 I. Fdez. Galván, M. G. Delcey, T. B. Pedersen, F. Aquilante and R. Lindh, *J. Chem. Theory Comput.*, 2016, **12**, 3636–3653.

26 A. Hjorth Larsen, J. Jørgen Mortensen, J. Blomqvist, I. E. Castelli, R. Christensen, M. Dułak, J. Friis, M. N. Groves, B. Hammer, C. Hargus, E. D. Hermes, P. C. Jennings, P. Bjerre Jensen, J. Kermode, J. R. Kitchin, E. Leonhard Kolsbjerg, J. Kubal, K. Kaasbjerg, S. Lysgaard, J. Bergmann Maronsson, T. Maxson, T. Olsen, L. Pastewka, A. Peterson, C. Rostgaard, J. Schiøtz, O. Schütt, M. Strange, K. S. Thygesen, T. Vegge, L. Vilhelmsen, M. Walter, Z. Zeng and K. W. Jacobsen, *J. Phys. Condens. Matter*, 2017, **29**, 273002.

27 S. Sen and I. Schapiro, *Mol. Phys.*, 2018, **116**, 2571–2582.

28 A. A. Granovsky, *J. Chem. Phys.*, 2011, **134**, 214113.

29 T. Shiozaki, W. Győrffy, P. Celani and H.-J. Werner, *J. Chem. Phys.*, 2011, **135**, 081106.

30 G. M. J. Barca, C. Bertoni, L. Carrington, D. Datta, N. De Silva, J. E. Deustua, D. G. Fedorov, J. R. Gour, A. O. Gunina, E. Guidez, T. Harville, S. Irle, J. Ivanic, K. Kowalski, S. S. Leang, H. Li, W. Li, J. J. Lutz, I. Magoulas, J. Mato, V. Mironov, H. Nakata, B. Q. Pham, P. Piecuch, D. Poole, S. R. Pruitt, A. P. Rendell, L. B. Roskop, K. Ruedenberg, T. Sattasathuchana, M. W. Schmidt, J. Shen, L. Slipchenko, M. Sosonkina, V. Sundriyal, A. Tiwari, J. L. Galvez Vallejo, B. Westheimer, M. Włoch, P. Xu, F. Zahariev and M. S. Gordon, *J. Chem. Phys.*, 2020, **152**, 154102.

31 S. Vela and C. Corminboeuf, *Chem. – A Eur. J.*, 2020, **26**, 14724–14729.

32 *Gaussian 16, Revis. B.01*, Gaussian, Inc., Wallingford CT, 2016.